

Geomagnetic Activity during Alaska's 2015 Autumn

Whitham D. Reeve

Abstract: The solar wind and all disturbances within it, including coronal hole high-speed streams, corotating interaction regions, solar sector boundaries, coronal mass ejections and other transient magnetic phenomena, constitute *space weather*. There also are other Sun-caused events and phenomena in the solar wind that do not fit into these neat categories. Because the Sun's magnetic field is embedded in the solar wind, space weather disturbances can strongly affect Earth's magnetosphere. The autumn in Alaska saw considerable geomagnetic activity caused by these phenomena.

Abbreviations:

AU: Astronomical Unit
CHSS: Coronal Hole High-Speed Stream
CIR: Corotating Interaction Region
CME: Coronal Mass Ejection
HCS: Heliospheric Current Sheet
IMF: Interplanetary Magnetic Field
NOAA: National Oceanic and Atmospheric Administration
SI: Sudden Impulse
SIR: Stream Interaction Region
SSBC: Solar Sector Boundary Crossing
SSC: Storm Sudden Commencement
SWPC: Space Weather Prediction Center

Geomagnetic activity shows a peak around the equinoxes. The autumn effect combined with the formation of low-latitude, Earth-directed coronal holes associated with the declining solar cycle led to what seemed like an almost continuous procession of geomagnetic storms. This paper provides a brief tutorial on solar and geomagnetic effects in Part I and then discusses geomagnetic observations at Anchorage, Alaska USA during September, October and November 2015 in Part II. This paper does not cover other space weather effects such as solar flares and associated radio blackouts or energetic particle events and their effects. For a geomagnetism tutorial see {[GeoMag](#)}.

Note: References in brackets [] and internet links in braces { } for Part I are listed in **section 1.9**.

Part I ~ Concepts

1.1. Solar Wind

The solar wind is an outward flow of plasma from the Sun that has been accelerated by the pressure gradient between the solar corona and the much lower pressure of interplanetary space. The plasma is mostly ionized hydrogen atoms and electrons. The radial flow speed of the *ambient* solar wind is about 450 km/s but the wind speeds measured outside the Earth's magnetosphere can vary by factors of 1/4 to 4 (or more) times the ambient during disturbed conditions. At Earth the wind direction is approximately 45° to the Sun-Earth line because of the way the wind spirals like a lawn sprinkler due to the Sun's rotation (figure 1.1).

The Sun's magnetic field is quite strong, varying from a few hundred thousand nT at the poles to 300 million nT at sunspots. The solar wind flow carries with it part of the Sun's magnetic field, often described as a "frozen-in" magnetic field but formally called *interplanetary magnetic field* (IMF). At a distance of 1 astronomical unit (AU), the Sun's magnetic field is relatively weak, averaging about 6 or 7 nT. Earth's own magnetic field at its surface averages about 50 000 nT but at the sunlit edge of its magnetosphere (the magnetopause) Earth's field is comparable to the IMF. These values seem miniscule but the energy involved in the IMF is massive.

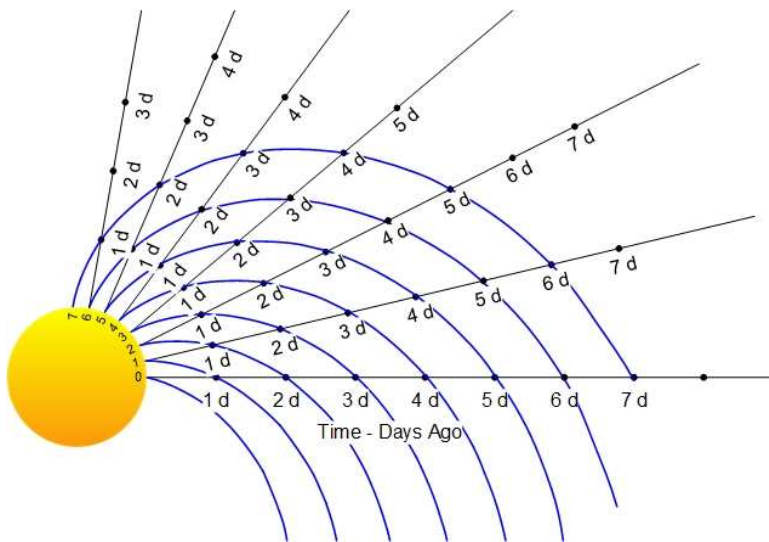


Figure 1.1 ~ Because of the Sun's rotation, the solar wind is like a lawn sprinkler. The geometry is called Archimedes Spiral or Parker Spiral. This view is from above the Sun's equatorial plane and shows the path of seven parcels of plasma blown away on each of 7 days. The Sun rotates counter-clockwise, and time is shown as days ago. Day 0 is today. The radial velocity of each parcel in the ambient solar wind is around 450 km/s. In one day (1 d) a parcel has traveled outward about 39 million km and it reaches Earth in about 3.9 d at an angle of 45° with respect to the Earth-Sun line. Image © 2015 W. Reeve.

1.2. Coronal Holes and High-Speed Streams

Coronal holes are areas on the Sun with a lower temperature and density compared to the surrounding corona. When instruments sensitive to EUV (extreme ultraviolet) and x-ray radiation are used to view the Sun, coronal holes appear as dark areas on the Sun's surface (figure 1.2). Coronal holes correspond to regions in which the Sun's magnetic field lines are open allowing them to extend to interplanetary space before looping back (figure 1.3). Because the Sun's magnetic field is relatively unconstrained in these areas, the solar wind blowing from them has higher speeds and temperatures. These streams are called *coronal hole high-speed streams* (CHSS).

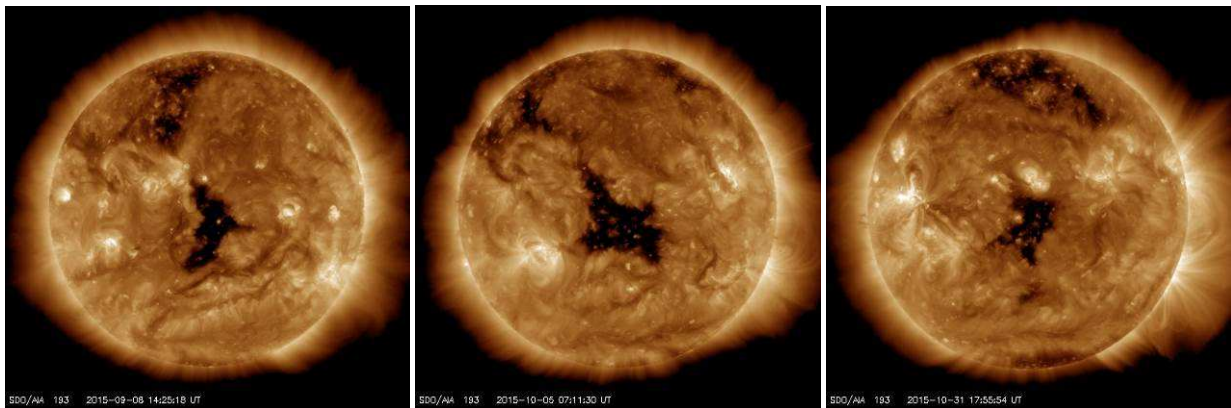


Figure 1.2 ~ Coronal holes appear as dark areas on the Sun's corona when imaged at 193 Å (19.3 nm) wavelength. These three images show a persistent coronal hole over two solar rotations (each rotation is approximately 27 d). Images were taken by the Solar Dynamics Observatory spacecraft Atmospheric Imaging Assembly (AIA) on 8 September, 5 October and 31 October 2015. Image courtesy of SDO/AIA.

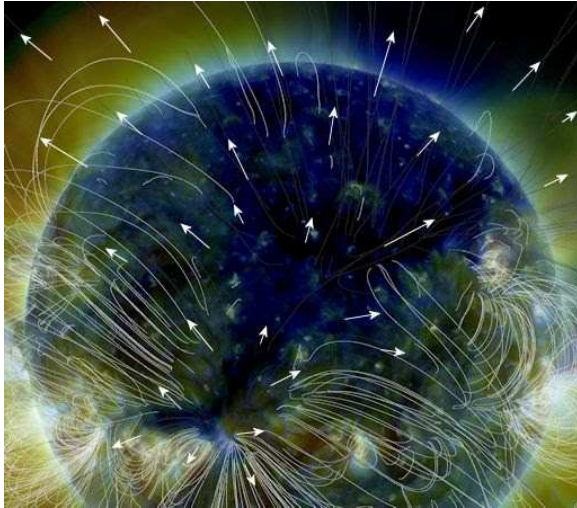


Figure 1.3 ~ Annotated image of the Sun showing magnetic field lines (faint gray lines) and outflowing stream (arrows) from a coronal hole. Image courtesy of SDO/AIA.

Coronal holes form and persist in the Sun's polar regions around solar cycle minimum and last for about 7 years. As the solar cycle advances toward the next maximum, peaks and then falls back toward the next minimum, coronal holes form at all latitudes. The lower-latitude coronal holes do not last nearly as long as those in the polar regions, but when they do form, the associated high-speed streams can intercept Earth as it orbits the Sun.

Numerous coronal holes formed during the autumn of 2015, and these may be seen in individual images and movies produced by NASA's Solar Dynamics Observatory (SDO) spacecraft. Daily movies are accessible at [{SDOMovie}](#). Movies also can be assembled for other time frames at [{AIAMovie}](#). Coronal holes are most visible at 193 Å wavelength ("bronze" SDO images).

An example of coronal hole effects is the large trans-equatorial coronal hole that transited the Sun's central meridian on 4 October. Three days later the ACE spacecraft and then Earth encountered the high-speed stream, which peaked slightly above 800 km/s (figure 1.4). The CHSS caused strong geomagnetic storm effects that were detected at Anchorage, Alaska about noon (UTC) on 7 October (figure 1.5). The *WSA-Enlil* space weather model [{WSA-Enlil}](#) used by National Oceanic and Atmospheric Administration (NOAA) clearly shows the increased wind speed (figure 1.6). WSA-Enlil is a large-scale prediction model based on heliospheric physics. It is used by the Space Weather Forecast Office to predict solar wind features and Earth-directed coronal mass ejections that could cause geomagnetic storms. The model can be run as an online animation but only time-slices can be shown here. Images from the model are used here and in Part II to provide a quasi-3-dimensional view of the space weather.

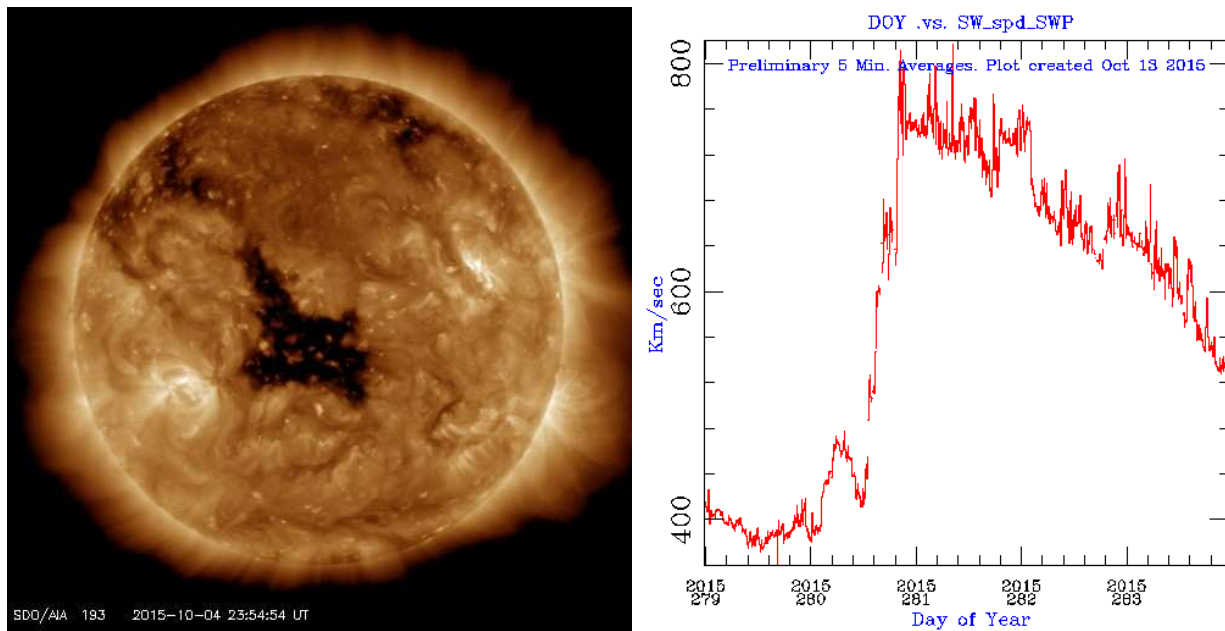


Figure 1.4 ~ Left: Large positive polarity coronal hole crossing the Sun’s central meridian on 4 October 2015 (the central meridian is the part facing Earth at any given time). It spans parts of the northern and southern hemispheres and is called trans-equatorial. Image made at 193 Å: Courtesy of SDO/AIA. Right: The solar wind speed recorded at the ACE spacecraft indicates a steep increase from 400 to 800 km/s about noon on 7 October (UTC day 280), 3 days after transit of the coronal hole. Image courtesy from ACE Science Center.



Figure 1.5 ~ Magnetogram from Anchorage, Alaska for 7 October. The day was magnetically very stormy starting mid-way through the 2nd synoptic period (0300 to 0600). The influence of the high-speed stream from the trans-equatorial coronal hole can be seen to start about 1200 and continue for over 8 h as Earth passed through it. The K-index shown along the top of the chart indicates the severity of the magnetic deviations during each 3 h synoptic period. For a description of the K-index, see [GeoMag](#).

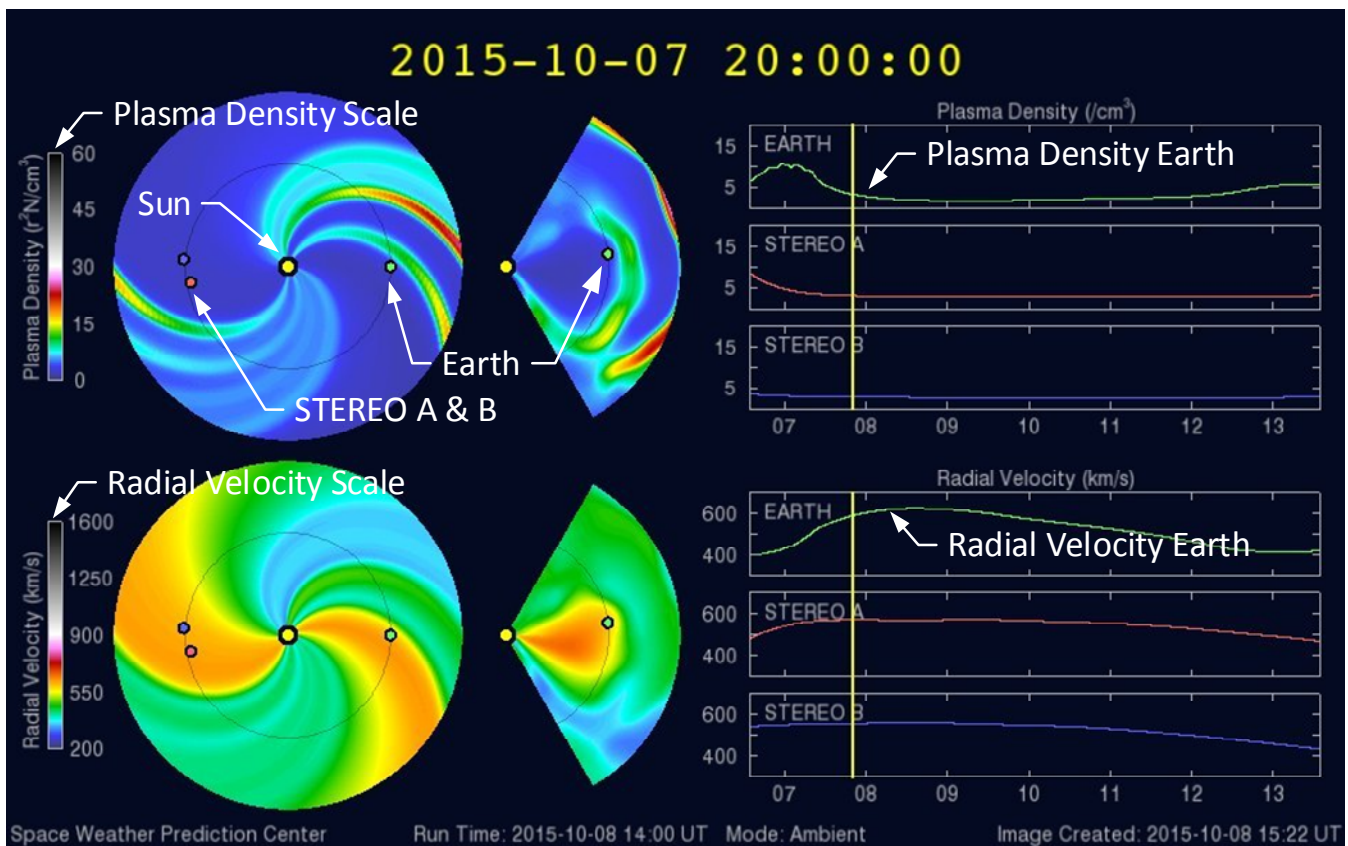


Figure 1.6 ~ Annotated WSA-Enlil Sun-Earth model of the coronal hole high-speed stream that affected Earth on 7 October 2015. The model is used by National Oceanic and Atmospheric Administration (NOAA) for space weather forecasting and shows the solar wind density (upper) and speed (lower) from the Sun to about 1.5 AU distance. The model usually shows data for 2 days before the current day and a forecast for 4 days after. The left circular images show the Sun at the center with Earth to the right as viewed from above Earth's orbital plane (the ecliptic). The two small globes to the left of center are the STEREO spacecrafts A and B. The pie images to the right of the overhead views show the Sun-Earth sector as seen from the orbital plane. The color scales on the far left indicate the solar wind plasma density and velocity. The corresponding plots for Earth and STEREO spacecraft on the right show the plasma density and radial velocity over an 8 h time period. The model is animated and can be set to run the full period. Underlying image courtesy of NOAA.

1.3. Corotating Interaction Regions

The higher speed coronal streams overtake the slower ambient solar wind. *Stream interaction regions* (SIR) form as the flow is compressed between the fast and slow wind components (figure 1.7). If a coronal hole persists over multiple solar rotations (a rotation takes approximately 27 days with the Sun's higher latitudes rotating slower than lower latitudes) the streams can form a *corotating interaction region* (CIR). The frozen-in magnetic field in a corotating interaction region is a complex mixture of magnetic field lines from the ambient solar wind and the higher speed streams.

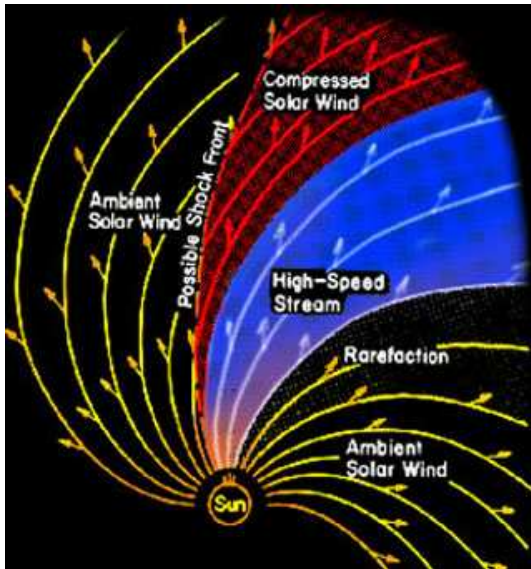


Figure 1.7 ~ High-speed solar wind plasma flows from the Sun overtake the slower ambient wind forming a compression region. If a compressed region persists for more than one solar rotation, it is called corotating interaction region. Image courtesy of NASA.

1.4. Solar Sector Boundary Crossing

As mentioned above, the solar wind has a spiral shape as it extends out from the Sun due to the Sun's rotation. Along the Sun's magnetic equator the field lines with opposite polarity are parallel. This creates a spinning current sheet about 30 000 km thick between the two polarities called the *heliospheric current sheet* (HCS) (figure 1.8). The current sheet behaves according to Ampere's law and carries a current on the order of a billion amperes. Because the Sun's rotational and magnetic axes are not always aligned, the current sheet is warped and develops folds, or sectors (figure 1.9). Along the plane formed by Earth's path as it orbits the Sun, the interplanetary magnetic field generally organizes itself into 2 or 4 sectors per solar rotation. When Earth crosses one of these folds, called a *solar sector boundary crossing* (SSBC), there is a change in the solar wind's magnetic polarity.

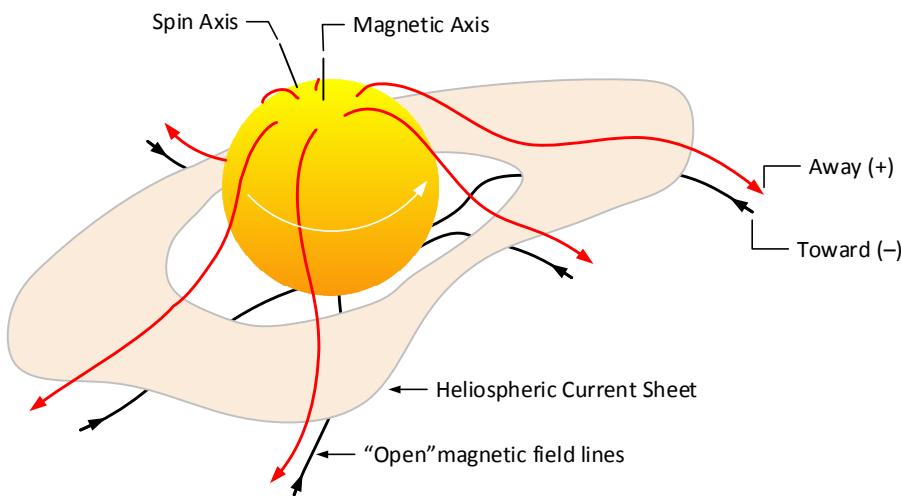


Figure 1.8 ~ A heliospheric current sheet exists between opposite polarity interplanetary magnetic field lines along the plane of the Sun's magnetic equator. The field lines are flattened because the solar wind carries them away as the Sun rotates. The Sun's magnetic and rotation axes are not always aligned so the sheet wobbles over time and folds form. Image adapted from [Smith78]

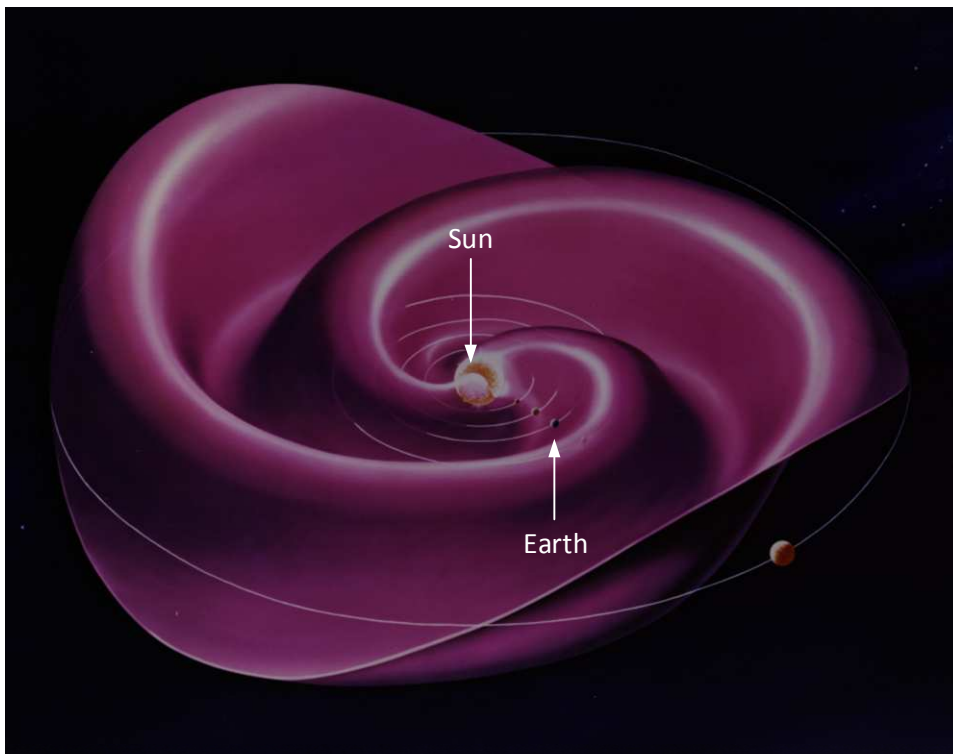


Figure 1.9 ~ The Sun is shown at the center of this image. Folds in the heliospheric current sheet called solar sector boundaries develop because the Sun's magnetic and rotational axes change alignment as the Sun rotates. The contours of the folds look similar to a twirling ballerina's skirt. When Earth crosses one of these folds, it is called a solar sector boundary crossing. The IMF's magnetic polarity outside of Earth's magnetosphere changes and has possible geomagnetic effects. Image adapted from: {SSBC}

1.5. Coronal Mass Ejections

A coronal mass ejection (CME) involves a huge mass of magnetized plasma blown into interplanetary space from the Sun's corona over a period of a few hours (figure 1.10). It is caused by instabilities and energy releases in the Sun's magnetic field and when imaged at EUV and x-ray wavelengths it appears as a huge, rapidly expanding bubble. The estimated mass in CMEs range from about 10^{12} to 10^{14} kg, roughly the mass of Denali, North America's highest mountain located in Alaska. Coronal mass ejection speeds can vary over a wide range from < 100 km/s (slower than the ambient wind) to > 2000 km/s. For comparison, a typical passenger jet flies about 0.2 km/s. Additional data and images of CMEs are available at [{Cactus}](#).

Not all CMEs are Earth-directed but the ones that are can cause significant geomagnetic effects. Coronal mass ejections are often associated with solar flares and prominence eruptions but not always. The frequency of CMEs varies with the Sunspot Numbers throughout the solar cycle (figure 1.11). Observations from spacecraft indicate about one CME per week at solar minimum and about two to three per day at solar maximum. An interesting movie of one full month of CMEs (but not in this paper's study period) can be downloaded [{CMEMon}](#).

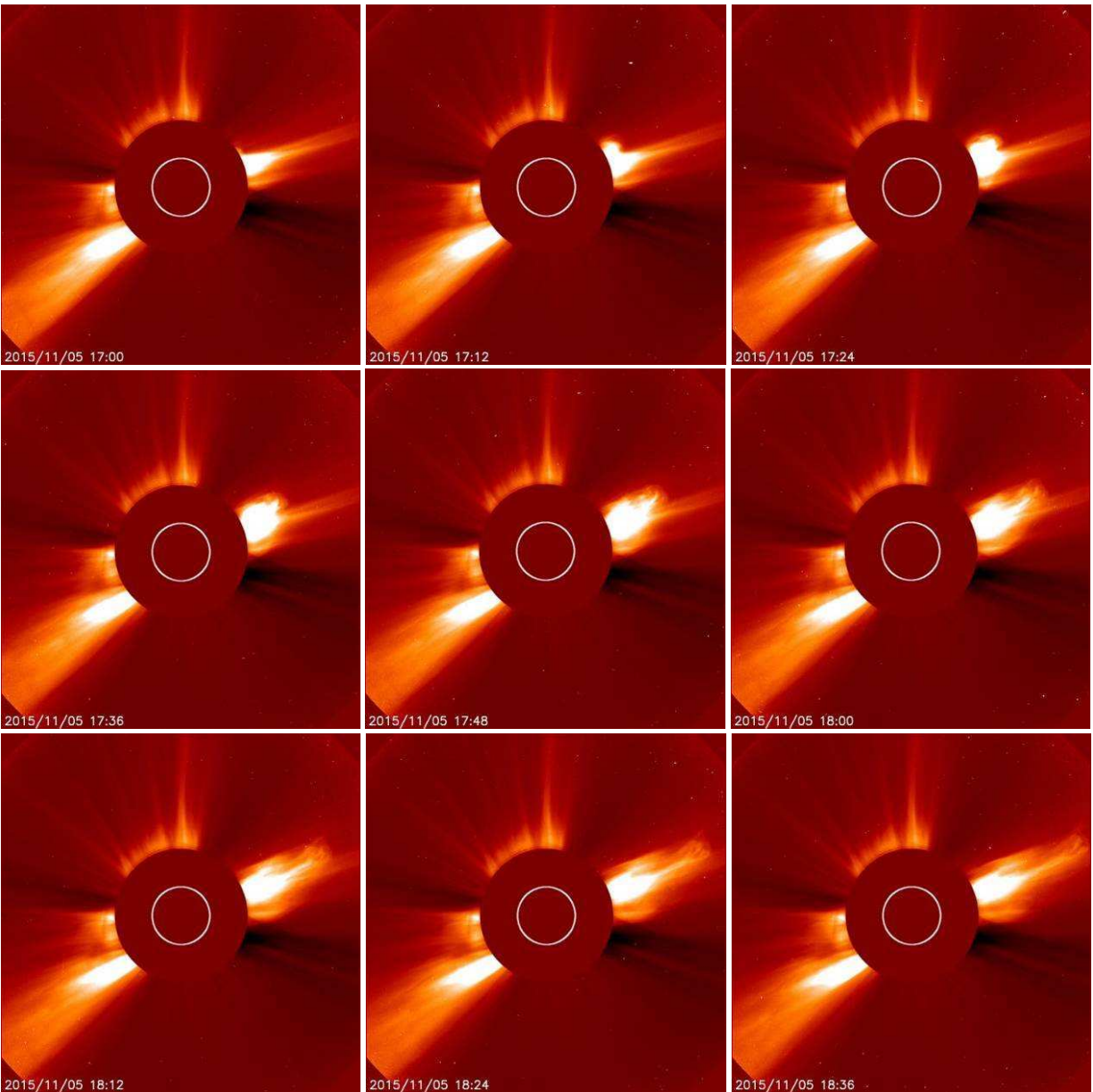


Figure 1.10 ~ Sequence of images from the LASCO C2 white light coronagraph on the Solar and Heliospheric Observatory (SOHO) spacecraft showing a CME on the right just above center of each image. The sequence starts at upper-left at 1700 on 5 November 2015. Images are spaced 12 minutes apart. The occulting disk in the coronagraph blocks the Sun's radiation. The white circle at center shows the background Sun. Images courtesy of NASA/SOHO.

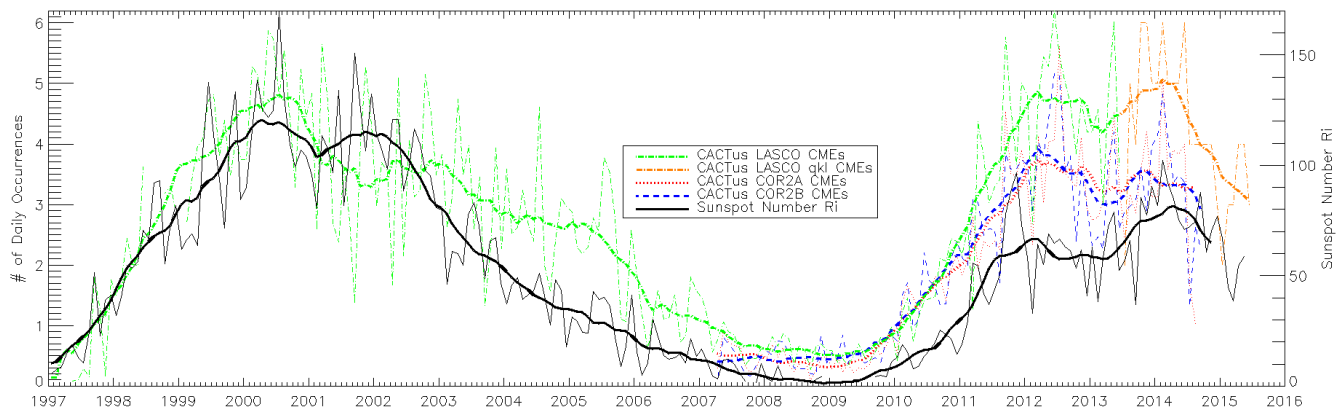


Figure 1.11~ Comparison of CME counts from various space platforms between 1997 and mid-2015 and the Sunspot Number (SSN). A solar cycle is roughly 11 years. The Sunspot Number is shown by the thin and thick solid black lines and CME counts by other colors. Thin lines are actual counts and thicker lines are smoothed. As this article was being written (November 2015), solar cycle 24 was in its descending phase. Image source:

http://sidc.oma.be/cactus/catalog/LASCO/2_5_0/dataoverview/CME_and_SSN_rate.png

CMEs leave a distinct magnetic shock signature on magnetometers as they pass. When a CME passes the Advanced Composition Explorer (ACE) spacecraft, which is located 1.5 million km from Earth along the Sun-Earth line, shock passage is indicated by a positive or negative rapid change or sudden perturbation of several nT in the data. The shock usually manifests itself a little later as a sudden impulse (SI) at Earth. Sudden impulse amplitudes usually are less than 50 nT. The magnetic field may or may not return to the pre-impulse level after the CME shock front passes. Sudden impulses have been called *Storm Sudden Commencement* (SSC) in the past because they often signified the beginning of a geomagnetic storm. Both the shock at ACE and SI on Earth are reported by Space Weather Prediction Center. A study of shocks and geomagnetic sudden impulses during the 12 month period 1 June 2012 through 1 June 2013 is discussed in {[ReeveSI](#)}.

1.6. Interplanetary Magnetic Field

The interplanetary magnetic field is a vector (magnitude and direction). The IMF magnitude measured near Earth (but outside the magnetosphere) varies from 1 to 37 nT. The vector is separated into components for convenience of analysis. In the Geocentric Solar Magnetospheric (GSM) coordinate system, the components are labeled B_x , B_y and B_z (figure 1.12). (Note: These components have a different orientation than similarly named geomagnetic field components associated with the terrestrial geographic coordinate system.)

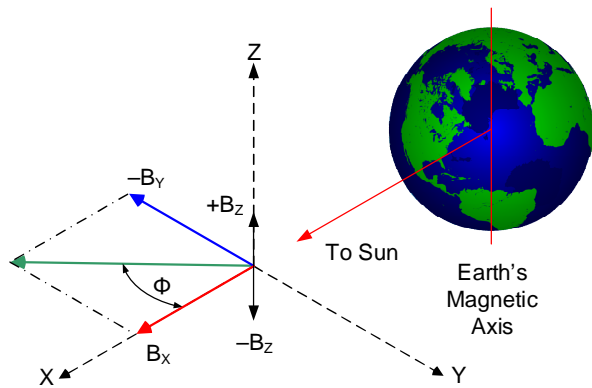


Figure 1.12 ~ Geocentric Solar Magnetospheric (GSM) coordinate system showing the B_x , B_y and B_z components and the angle Φ , which is determined by B_x and B_y . In this illustration, Φ is approximately 315° so it is reported as in the negative sector and toward the Sun. When the B_z component is pointed up (north) it is positive and when pointed down (south) it is negative. The GSM coordinate system is centered on Earth but shown here as external for clarity. Image © 2015 W. Reeve.

Even though the Sun's magnetic field lines are radial at its equator, in interplanetary space the field has a vertical component B_z formed by waves, folds and disturbances in the solar wind. The B_z component is defined so that it aligns with Earth's magnetic dipole axis and is approximately perpendicular to the plane formed by Earth's orbit (ecliptic). On a broad scale, B_z changes with the seasons as Earth orbits the Sun. B_z can point north or south with respect to Earth and is positive when pointed north. Variations of B_z generally are greater than variations of the other GSM components B_x or B_y .

The B_x and B_y components are parallel to Earth's orbital plane with $+B_x$ pointing from Earth to the Sun and $+B_y$ pointing to the left when looking at the Sun from Earth. The vector sum of B_x and B_y has an angle designated by the Greek letter phi, Φ . Φ is 0° when aligned with the x-axis and increases counter-clockwise when viewed from above. When between 0° and 180° Φ is reported in the positive sector (away from the Sun) and when between 180° and 360° it is reported in the negative sector (toward the Sun). Φ most often is about 135° or 315° (this is equivalent to the 45° angle of the spiral arms mentioned in section 1.1) depending on whether the IMF is toward or away from the Sun, respectively.

The Φ angle is important in space weather forecasting because it indicates how Earth is connected with the Sun in relation to the heliospheric current sheet. Around the fall equinox, coronal holes and transient events such as CMEs that originate in the Sun's positive hemisphere will be better connected and potentially have stronger effects on the Earth's magnetosphere. Similarly, during the spring equinox, coronal holes and CMEs with a negative polarity will have a better connection. These seasonal effects are described in detail in [Russell73](#).

1.7. Magnetic Reconnection and Disturbances

Space weather can strongly disturb Earth's magnetosphere depending on the polarity of the IMF's vertical component B_z and other factors. Earth's magnetic field closely approximates a dipole much like a bar magnet. The Earth's north *magnetic* pole has a south polarity. Above Earth's equator the lines of force from the geomagnetic field point north. When the B_z component of the solar wind has a significant southward magnitude (opposite to Earth's field), the Sun's magnetic field lines can connect with Earth's magnetic field lines because opposite magnetic poles attract. This process is called *reconnection*.

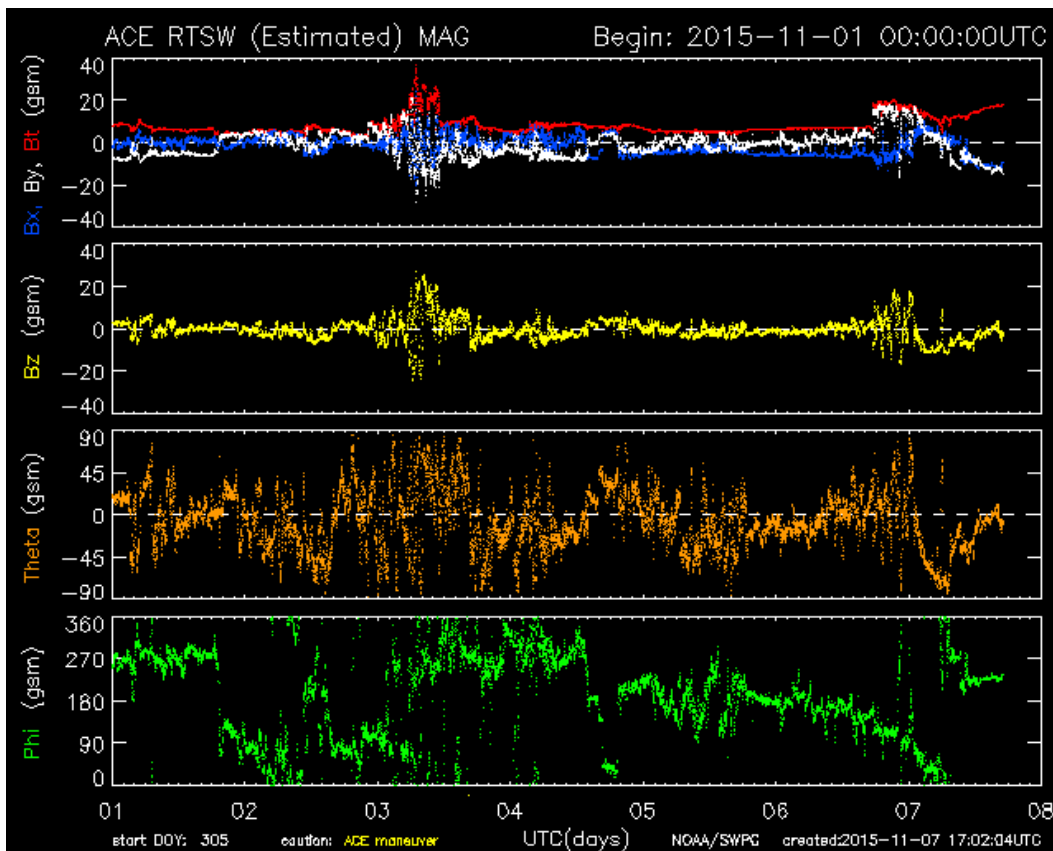


Figure 1.13 ~.7-day plot of data received from the ACE spacecraft on 1 November. The upper plot shows B_x , B_y and B_T (The total field B_T is the vector sum of B_x , B_y and B_z) and the next plot down shows B_z . Phi angle is shown in the bottom plot. Image courtesy of ACE Science Center.

The magnitudes and angles of the solar wind magnetic field components are measured at the ACE spacecraft (figure 1.13), which provides about 10 to 60 minute warning of oncoming space weather depending on its speed. Measurements of the angle Φ by ACE indicate the polarity of oncoming space weather and thus help forecasters judge how severely it will affect Earth. ACE also provides a lot of other data such as the solar wind density and speed. This data is incorporated in the WSA-Enlil space weather model to aid in forecasting solar wind density and speed as previously described. The forecasts are updated and issued by NOAA's Space Weather Prediction Center every 12 h {[SWPCFrst](#)}.

The solar wind distorts Earth's magnetosphere, compressing it on Earth's upwind day side and elongating it on the downwind night side (figure 1.14). The stretched out magnetosphere on the downwind side is called the magnetotail. The reconnection of the IMF with Earth's magnetic field dumps a huge amount of magnetic energy into Earth's magnetosphere where it is converted to kinetic and thermal energy and particle acceleration. This energy is carried to the magnetotail and, as it builds up, the environment becomes unstable, reaches a tripping point and the energy is released. At northern latitudes, this process can quasi-periodically repeat itself with characteristic times as short as a 1 or 2 h. The energy releases can cause large disturbances in Earth's magnetosphere that are manifested as geomagnetic storms.

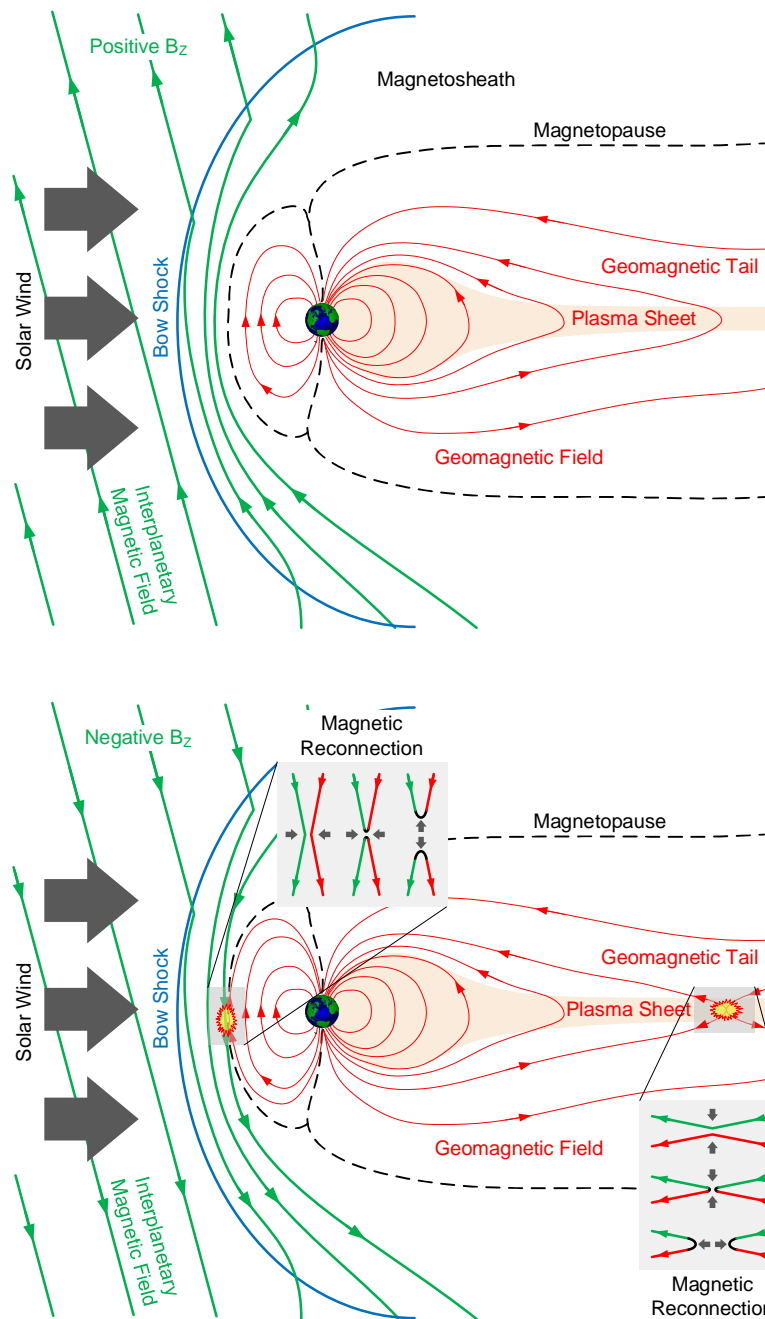


Figure 1.14 ~ A slice of Earth's 3-dimensional magnetosphere showing magnetic field lines associated with Earth and the solar wind as viewed from Earth's orbital plane. The Sun is to the left out of view and Earth is the small circle near the center. The magnetopause is where the magnitude of Earth's magnetic field is the same as the IMF. The Van Allen radiation belts and plasmasphere are not shown.

Upper: Conceptual drawing showing the vertical component of the interplanetary magnetic field (green) in the same direction as Earth's magnetic field (red) and no reconnection occurs. When the IMF is pointed southward, opposite to Earth's field, reconnection occurs and energy is dumped into the magnetosphere.

Lower: Conceptual drawing identical to above except the vertical component of the IMF is opposite to Earth's magnetic field. In this situation, magnetic reconnection can occur on the day side at the bow of the magnetopause. As the magnetic energy from this process is blown around Earth and converted to kinetic energy and heat, reconnection can occur in the magnetotail resulting in plasma moving rapidly toward Earth.

Illustrations adapted from NASA image with reconnection inserts adapted from [Murphy]

Geomagnetic storms can cause many problems both on Earth's surface and in spacecraft (figure 1.15). Storms induce anomalous currents in terrestrial power system transmission lines; damage power system transformers due to induced harmonic and direct currents; induce currents in underground pipelines that increase galvanic corrosion; cause electronic systems failures in spacecraft as well as increase the attenuation and scintillation of satellite signals (GNSS and communications satellites) as they pass through the ionosphere. Other effects are increased biological risks that include exposing airline flights over Earth's polar regions to higher radiation levels. High levels of geomagnetic activity also cause aurora – commonly called Northern Lights and Aurora Borealis in the northern hemisphere and Southern Lights and Aurora Australis in the southern hemisphere.

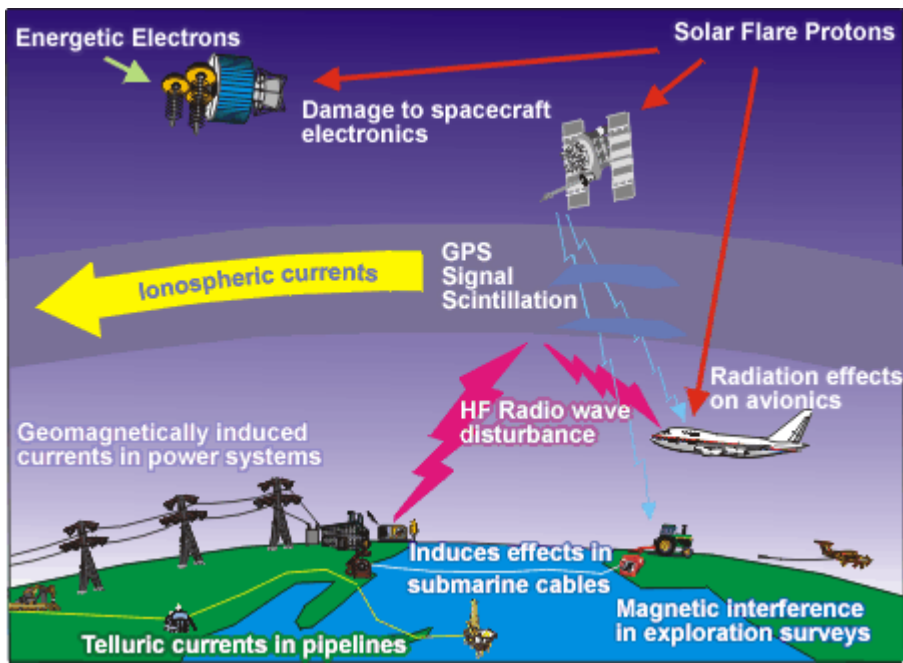


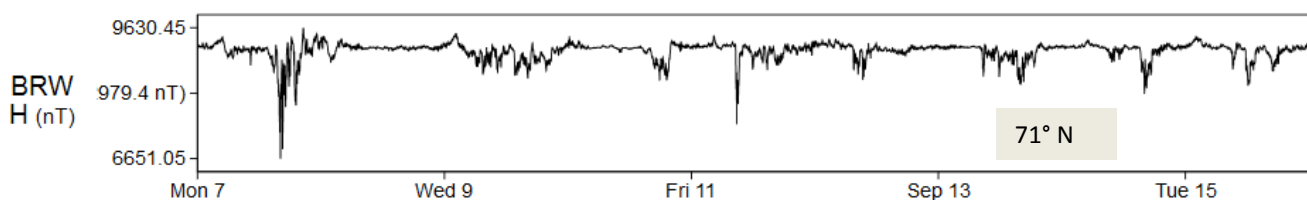
Figure 1.15 ~ Effects of solar activity and related geomagnetic storms. Image source: NASA

The intensities of disturbances to Earth's magnetic field vary over a wide amplitude and time range. Several methods have been devised to categorize the disturbances similar to terrestrial weather storm scales. One such categorization is based on the 10-level K-index, which measures the amplitude variation of the Earth's magnetic field horizontal component in each of eight 3-hour synoptic periods (0000 to 0300 UTC, 0300 to 0600 and so on). Generally, a K-index of 5 (K5) and higher is considered a geomagnetic storm. Space weather is reported by NOAA in terms of a Geomagnetic Scale (G-scale), which is related to the planetary K-index, Kp. The planetary index, Kp, is an average of many stations. See {[NOAA-G](#)}.

1.8. Variation of Geomagnetic Effects with Latitude

The magnitude of geomagnetic variations increases with latitude. Higher latitudes, above about 60°, have a higher level of natural activity and any disturbances have a greater magnitude (figure 1.15). These natural variations with latitude are taken into the account when the K-index at a given station is determined. There also are variations with longitude but they are mostly due to the local environment and day and night effects.

All measurements discussed in Part II of this paper were made at Anchorage, Alaska, which is near the southern edge of the auroral oval (figure 1.16).



40° N

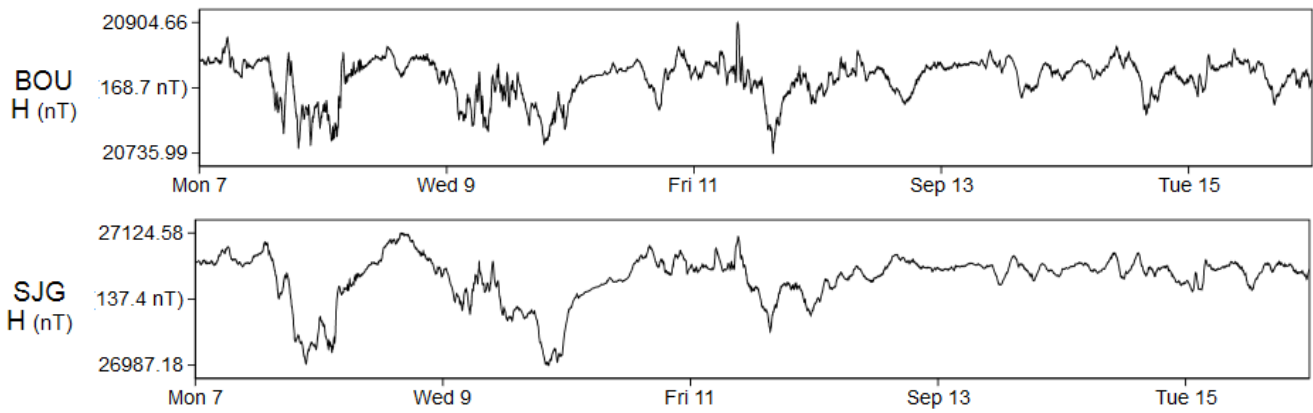


Figure 1.15 ~ Horizontal component (vector sum of terrestrial B_x and B_y) of Earth's magnetic field recorded at Barrow (BRW, Alaska, 71° N), Boulder (BOU, Colorado, 40° N) and San Juan (SJG, Puerto Rico, 18° N) between 7 and 16 September 2015. .Note the vertical scale ranges are different for each location, varying from 980 nT at Barrow to 137 nT at San Juan (plots are auto-scaled by the web application that produces them). Plots courtesy of USGS. Real-time and historical plots are available at {USGS}.

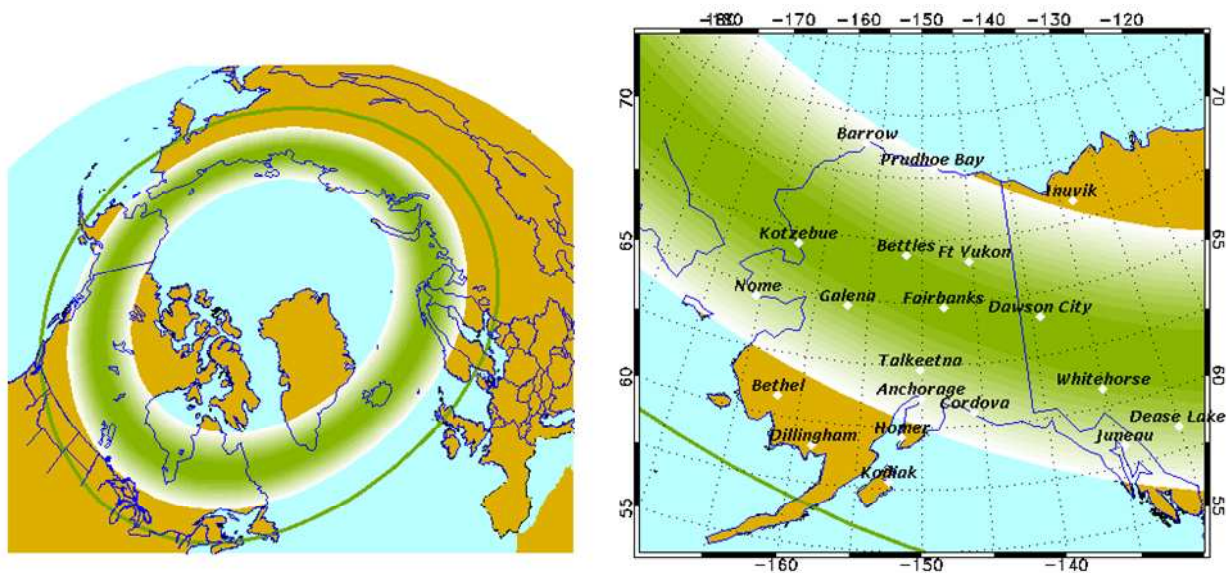


Figure 1.16 ~ Anchorage is near the southern edge of the auroral oval. These images show the forecast for aurora viewing on 30 November when the oval was expanded by a geomagnetic disturbance associated with a corotating interaction region followed by positive polarity coronal hole high-speed stream. Images courtesy of University of Alaska – Fairbanks, Geophysical Institute.

1.9. References and Further Reading for Part I

[Murphy] Murphy, N., Magnetic Reconnection, Harvard-Smithsonian Center for Astrophysics, Astronomy 253: Plasma Astrophysics, April 2014, available here:
http://www.cfa.harvard.edu/~namurphy/Lectures/Ay253_10_Reconnection.pdf

- [[Smith78](#)] Smith, E and Tsurutani, B., Observations of the Interplanetary Sector Structure up to Heliographic Latitudes of 16°: Pioneer 11, Journal of Geophysical Research, Vol. 83, No. A2, February 1, 1978, available here: www.leif.org/EOS/JA083iA02p00717.pdf
- [[ReeveS1](#)] Reeve, W., Geomagnetic Sudden Impulses, 2013, available here: http://www.reeve.com/Documents/Articles%20Papers/Observatoins/Reeve_GeomagSuddenImpulses.pdf
- {[Russell73](#)} Russell, C. and McPherron, R., Semiannual Variation of Geomagnetic Activity, Journal of Geophysical Research, Vol. 78, Iss. 1, pg 92-108, 1973, available here: <http://www-ssc.igpp.ucla.edu/personnel/russell/papers/40/>
- {[GeoMag](#)} Reeve, W., Geomagnetism Tutorial, 2011, available here: <http://www.reeve.com/Documents/SAM/GeomagnetismTutorial.pdf>
- {[AIAMovie](#)} <http://sdo.gsfc.nasa.gov/data/aiahmi/>
- {[Cactus](#)} <http://www.sidc.oma.be/cactus/out/CME0020/CME.html>
- {[CMEMon](#)} http://solarscience.msfc.nasa.gov/images/c2_1mth.mpg
- {[NOAA-G](#)} <http://www.swpc.noaa.gov/noaa-scales-explanation>
- {[SSBC](#)} <http://wso.stanford.edu/SB/SB.html>
- {[SWPCFrcst](#)} <http://www.swpc.noaa.gov/products/forecast-discussion>
- {[WSA-Enlil](#)} <http://www.swpc.noaa.gov/products/wsa-enlil-solar-wind-prediction>
- {[USGS](#)} <http://geomag.usgs.gov/plots/>
- Knipp, D., Understanding Space Weather and the Physics Behind It, Space Technology Series, Learning Solutions, McGraw-Hill Book Co., 2011
- Moldwin, M. An Introduction to Space Weather, Cambridge University Press, 2008

Part II ~ Magnetic Observations at Anchorage, Alaska

2.1 Instrumentation

All measurements were produced by a SAM-III three-axis magnetometer between 1 September and 30 November 2015 at Anchorage, Alaska (figure 2.1):

Geographic: 61.199° N 149.957° W
Geomagnetic (IGRF 2015): 61.68° N 95.15° W

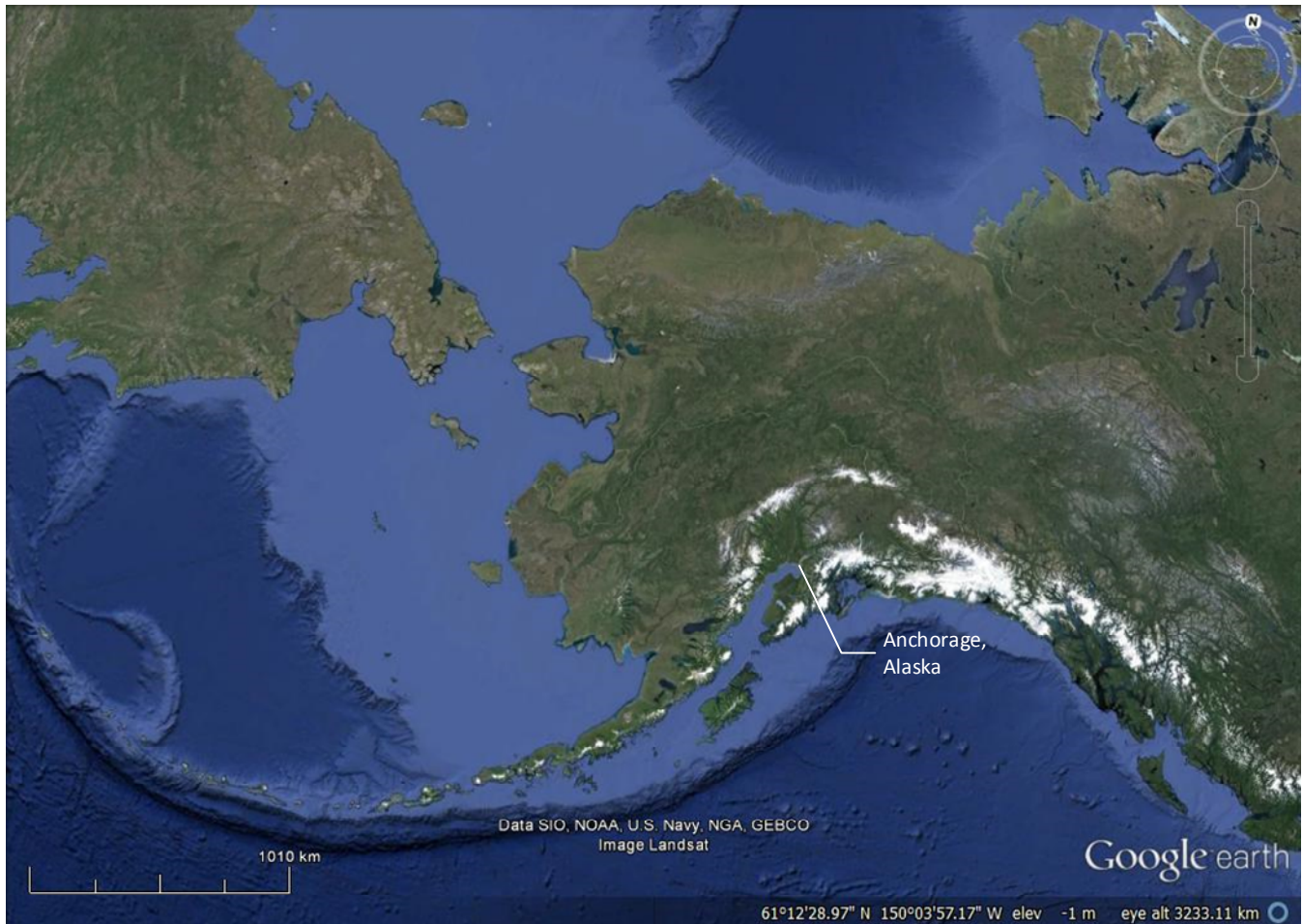


Figure 2.1 ~ Map of Alaska showing location of Anchorage SAM-III magnetometer. Image courtesy Google earth.

For further a description of the Anchorage SAM-III, see [\[ReeveSI\]](#).

Note: References in brackets [] and internet links in braces { } for Part II are listed in **section 2.5**.

A magnetogram shows the magnetic flux density (magnetic induction) with respect to time. SAM-III magnetograms typically are normalized at 2400 UTC and show magnetic variations relative to that time. However, the instrument saves the data as uncalibrated absolute values. For a more complete discussion of magnetograms, see [{GeoMag}](#).

The SAM-III produces one complete file of magnetic data each UTC day. In the case of the Anchorage instrument, the magnetic induction is measured and recorded at a 0.1 Hz rate and time-stamped by the PC's

time-of-day clock, which is synchronized to UTC with ± 10 ms accuracy. The data for the three axes (B_x , B_y and B_z in the terrestrial geographic coordinate system) are saved in ordinary space and comma delimited ASCII text files with the time stamps.

2.2 Data Reduction

The SAM-III data were imported to Excel software for post-processing. First, the data were resampled with a period of thirty 10 s intervals (300 s or 5 min). Next, the horizontal component, H, was calculated from the x- and y-components of the magnetic data. Plots of H were produced from the resampled data for each day and each of the three months as well as from a concatenation of data for the entire three month period. Resampling (or decimation) produces a lowpass filter effect, which tends to mask events with time scales shorter than the sampling period. However, most phenomena discussed here were caused by longer term disturbances. The exceptions are a few sudden impulses, which are analyzed using original data (not resampled data).

Some simple harmonic analyses of the data were performed as an afterthought using the *Fourier Analysis* function in Microsoft Excel's Data Analysis tool pack. A window (or tapering) function was not used, nor was any other processing except for determining the Fourier coefficient magnitudes from the complex results. In Excel the Fourier analysis is limited to 4096 data points, corresponding to a total time interval of about 14 days in each month for the decimated data.

2.3 Data Plots and Discussion

K-Index: The SAM-III software automatically calculates a local K-index for each 3-hour synoptic period and optionally shows it on the daily magnetogram. This actually is a pseudo-K-index because it is calculated on each of the X, Y and Z magnetic components instead of the horizontal component, H. In the individual daily plots shown here, the highest K-index of the three components is indicated at the top of the magnetogram (figure 2.1). During the 91 day study period, the K-index was K5 or higher (storm level by the definition discussed in Part I) for a total of 208 synoptic periods out of 728 total and equal to K9 (maximum possible) for 27 periods (figure 2.2).

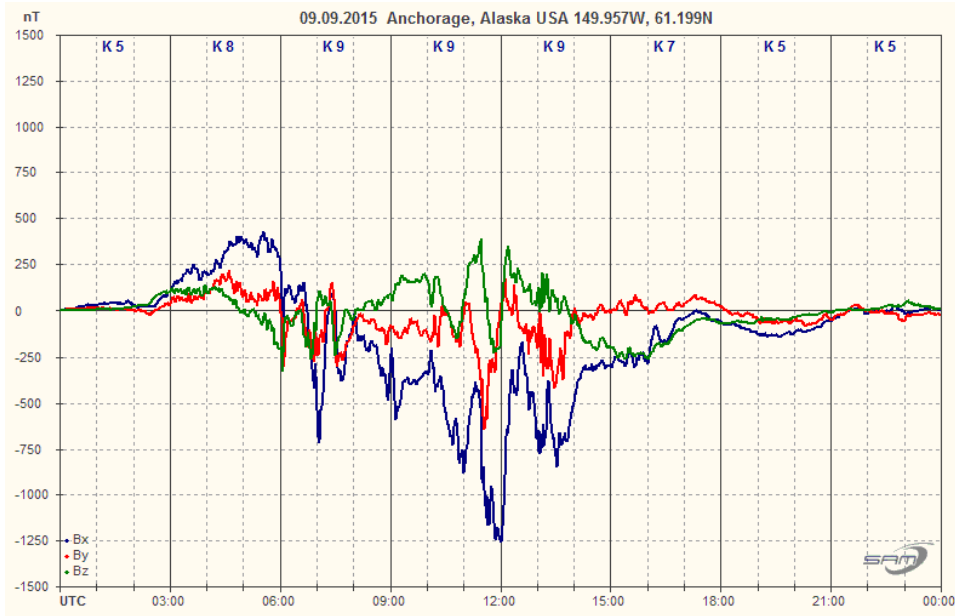
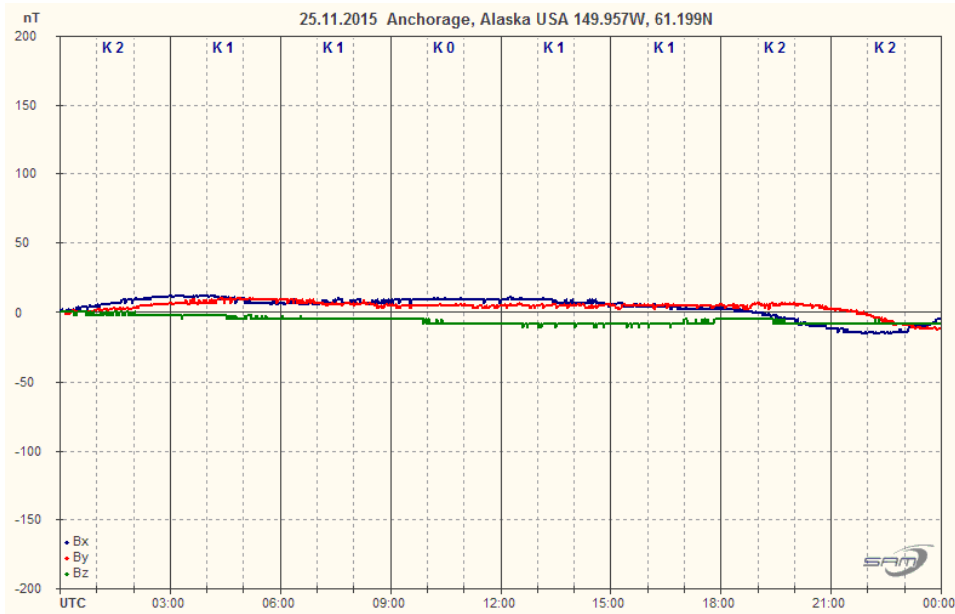


Figure 2.1 ~ Magnetograms showing K-index along the top of the chart for magnetically active and quiet days. Note the vertical scale differences between upper and lower plots.

Upper: The geomagnetic field was very active on 9 September with the K-index at or above storm levels for all eight of the 3-h synoptic periods. The disturbances were caused by a coronal hole high-speed stream and coronal mass ejection. The B_z component of the IMF rotated southward to -9 nT late in the prior day resulting in reconnection with Earth's magnetic field and the disturbances.



Lower: For comparison 25 November was magnetically very quiet.

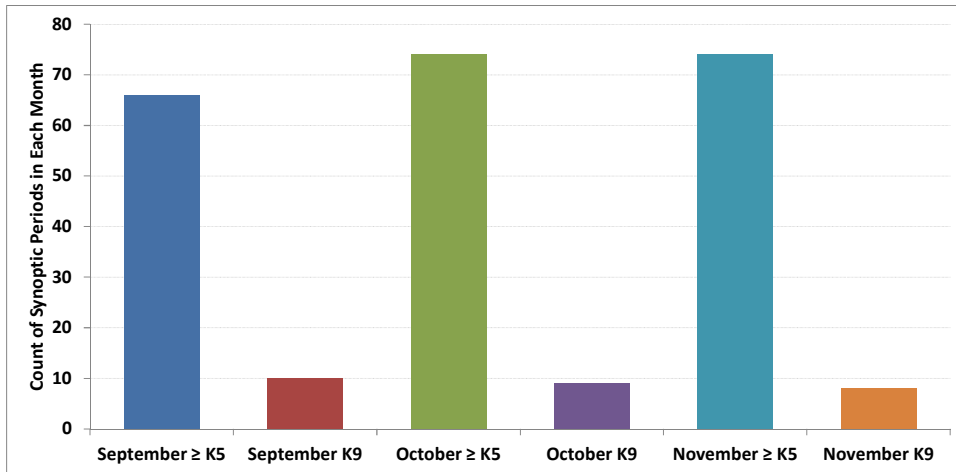


Figure 2.2 ~ Histogram of number of synoptic periods in each month in which the K-index was $\geq K5$ and $= K9$ during September, October and November 2015. Approximately 29% of all periods experienced K5 or greater and 4% experienced the highest possible K9.

Sudden impulses: Although the Sun threw off many coronal mass ejections during the study period (roughly 2 per day), only four of them caused a sudden impulse on Earth. On a 24-h magnetogram, the SI is seen as a short spike but on a shorter time-scale it is seen as a rapid positive or negative change lasting several minutes (figure 2.3). As mentioned in Part I, CMEs are responsible for shocks at the ACE spacecraft and sudden impulses on Earth (figure 2.4).

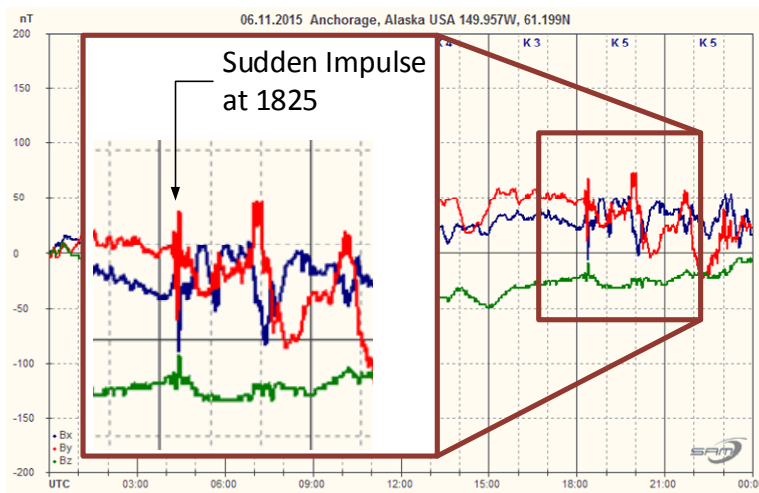
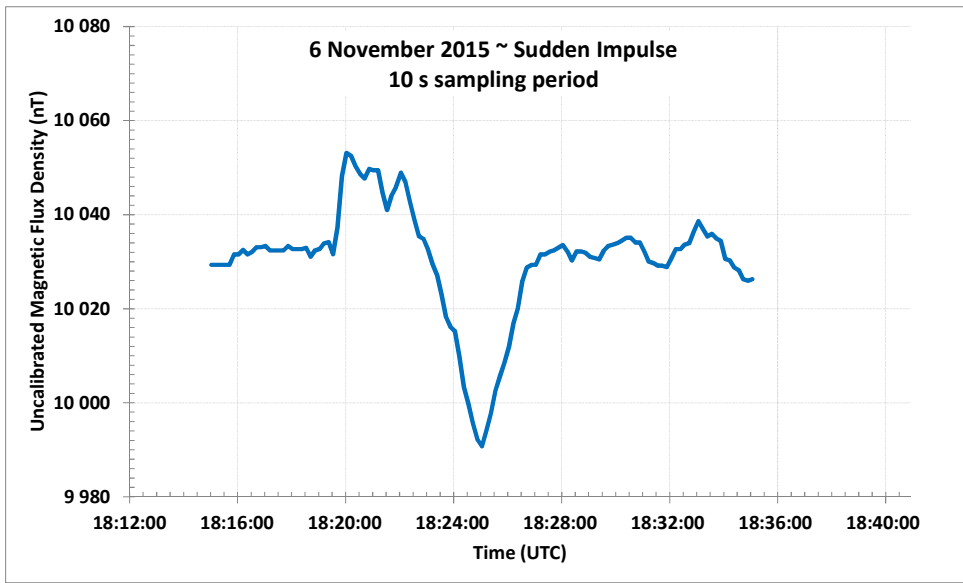


Figure 2.3 ~ One of four sudden impulses during the study period, this one from 6 November 2015. The Space Weather Prediction Center reported the event time as 1825; however, the Anchorage magnetometer recorded the event at 1820 (slight time differences around the world are not unusual).

Upper: Magnetogram showing the sudden impulse effects in all three axes: B_x : Blue; B_y : Red and



B_z: Green. The expanded area on left shows about 5 h. The SI is almost indistinguishable from the follow-on disturbances.

Lower: Plot of the original 10 s data for a period of about 10 min before and after the sudden impulse showing an initial positive pulse of 20 nT followed almost immediately by a larger negative dip of 60 nT and then recovery. The total impulse lasted almost 8 min.

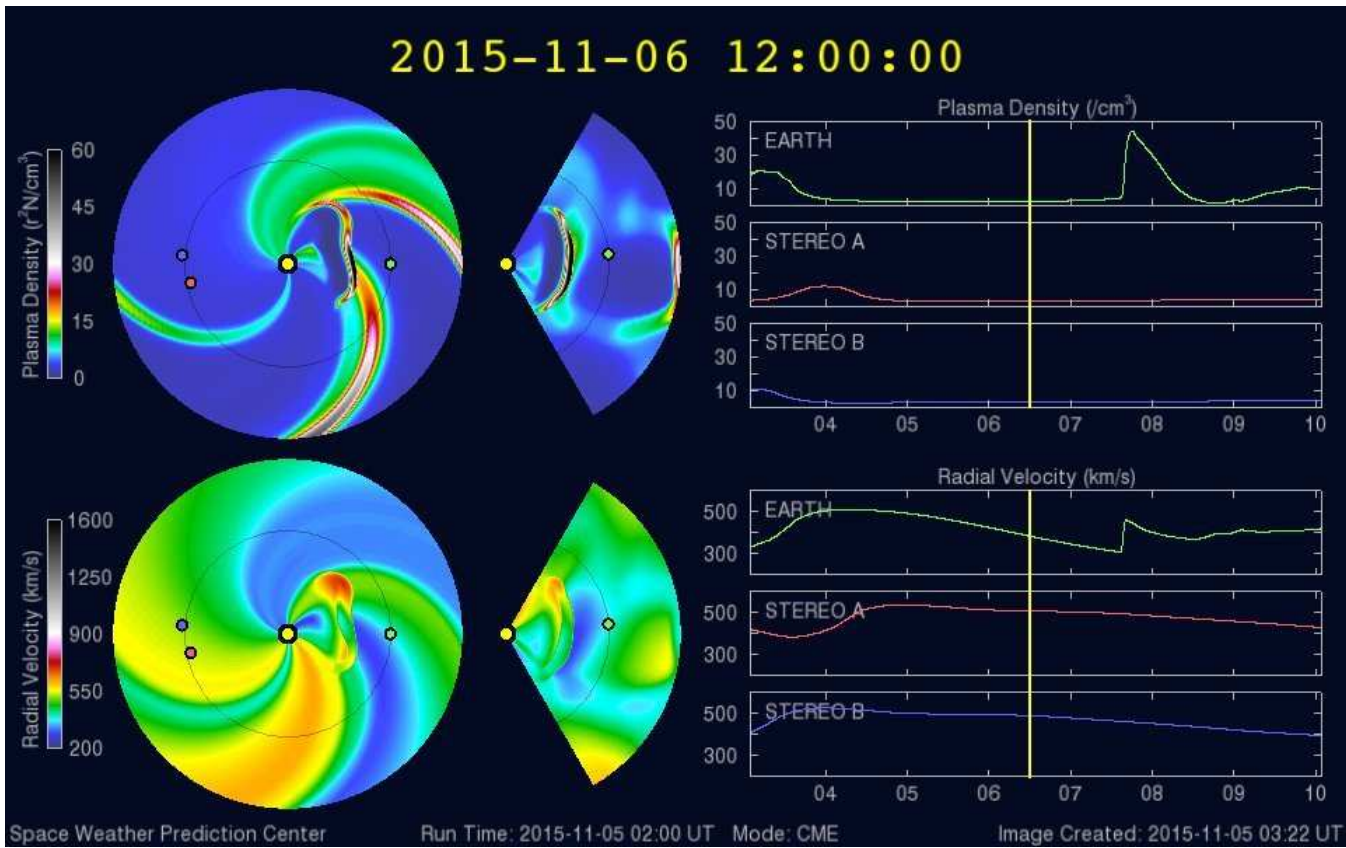


Figure 2.4 ~ Modeled results of the CME that hit Earth on 6 November at 1825. This snapshot shows the CME enroute to Earth and about half-way there. The corotating interaction region, which is modeled to reach Earth late on 7 November is indicated by the sharkfin shaped pulse in plasma density plot at upper-right, has been severely disturbed by the CME. Apparently, the model assigned too low of speed to the CME because it hit Earth about 6.5 h after this snapshot.

Daily magnetograms: The horizontal component, H, of Earth’s magnetic field at Anchorage, Alaska was calculated from the measured x- and y-components for each day and then plotted as overlays (figure 2.5). The vertical components, Z, for each day also are plotted as overlays (figure 2.6).

An interesting phenomenon is observed on the overlaid horizontal component plots: On days with magnetic disturbances, the disturbances most often were centered on noon UTC, which is approximately 0200 local Anchorage solar time. At this time Anchorage would be almost in line with the magnetotail where magnetic energy is being released due to reconnection. Also, almost all the major disturbances resulted in a decrease in the local horizontal magnetic flux density at Anchorage except for a few early in the UTC day. The vertical component has a wider dispersion of activity throughout the days with both increases and decreases in the magnetic flux density.

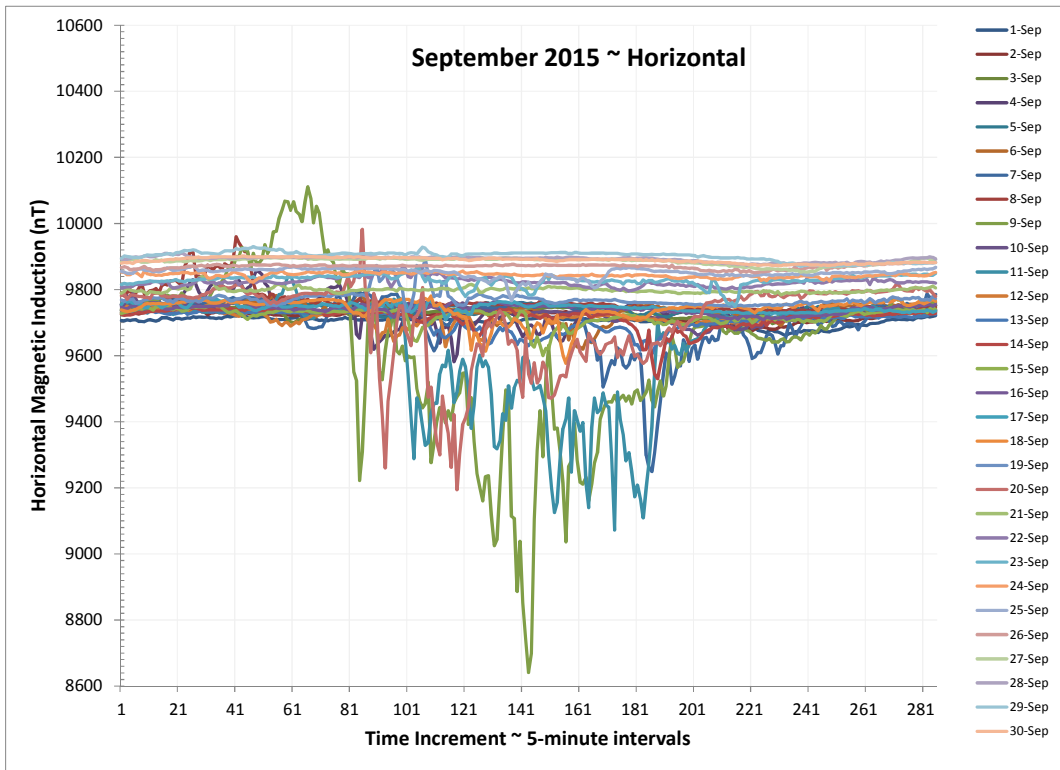
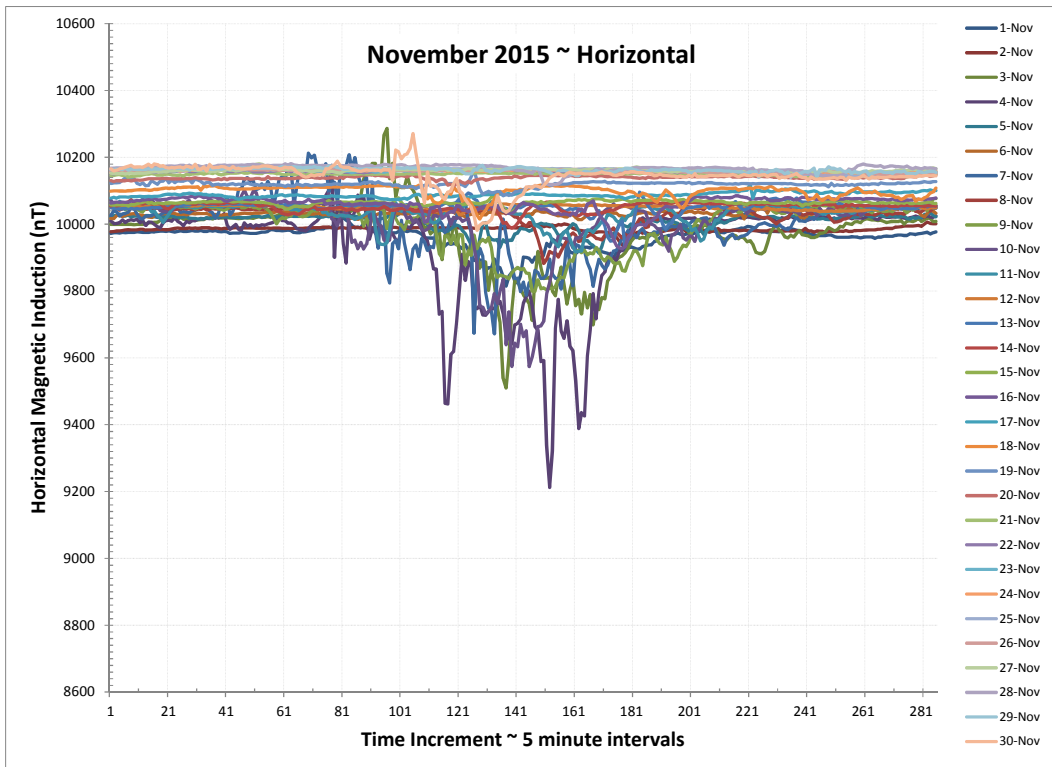
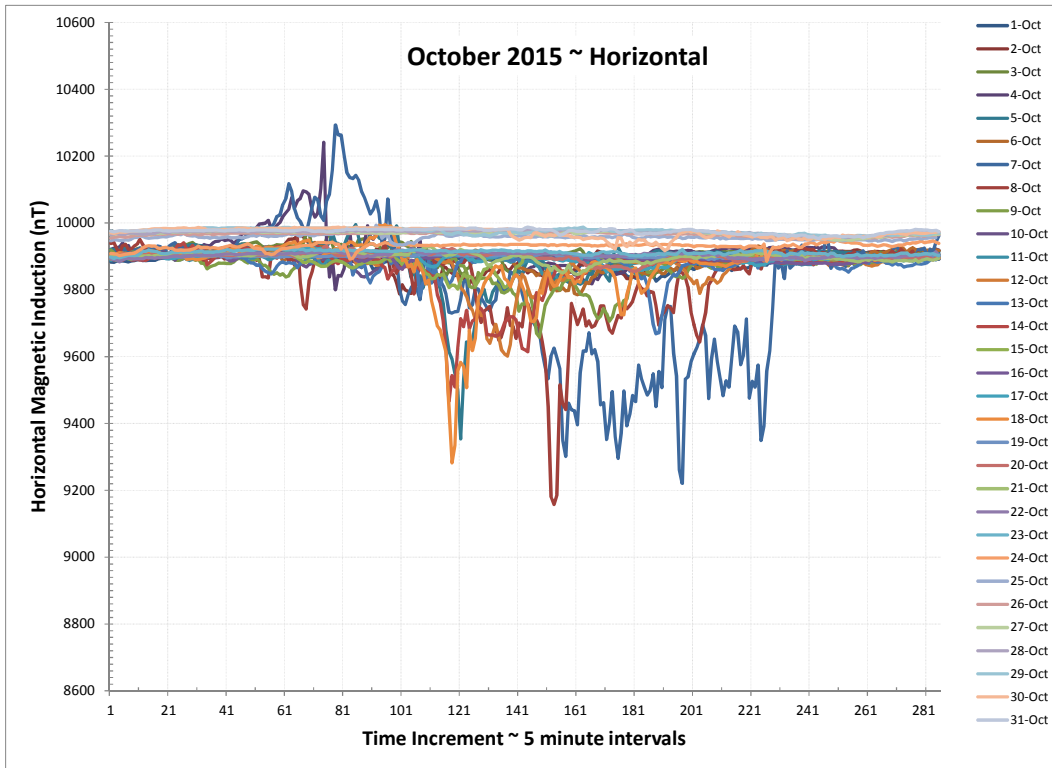


Figure 2.5 ~ Overlays of the daily horizontal magnetic flux density plots for each of the three months in the study period. The horizontal time scale on each plot is an index of 5 minute intervals. Major tick marks are at 100 min intervals. The vertical scales are uncalibrated values of the horizontal component (vector sum of B_x and B_y).



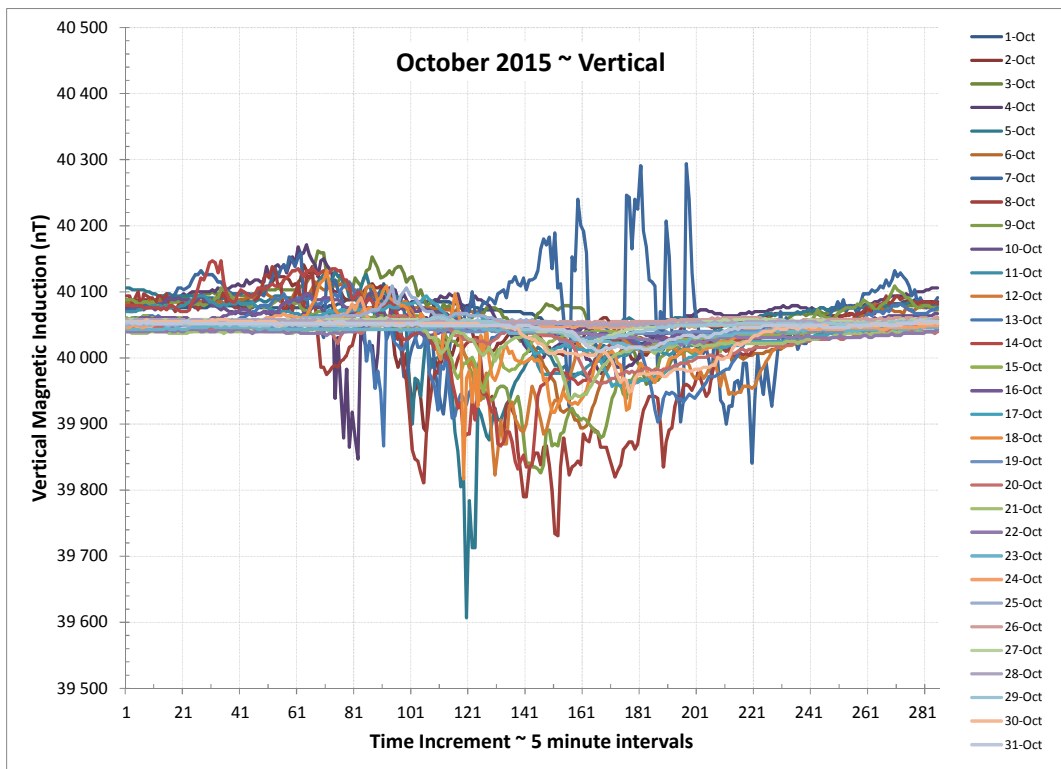
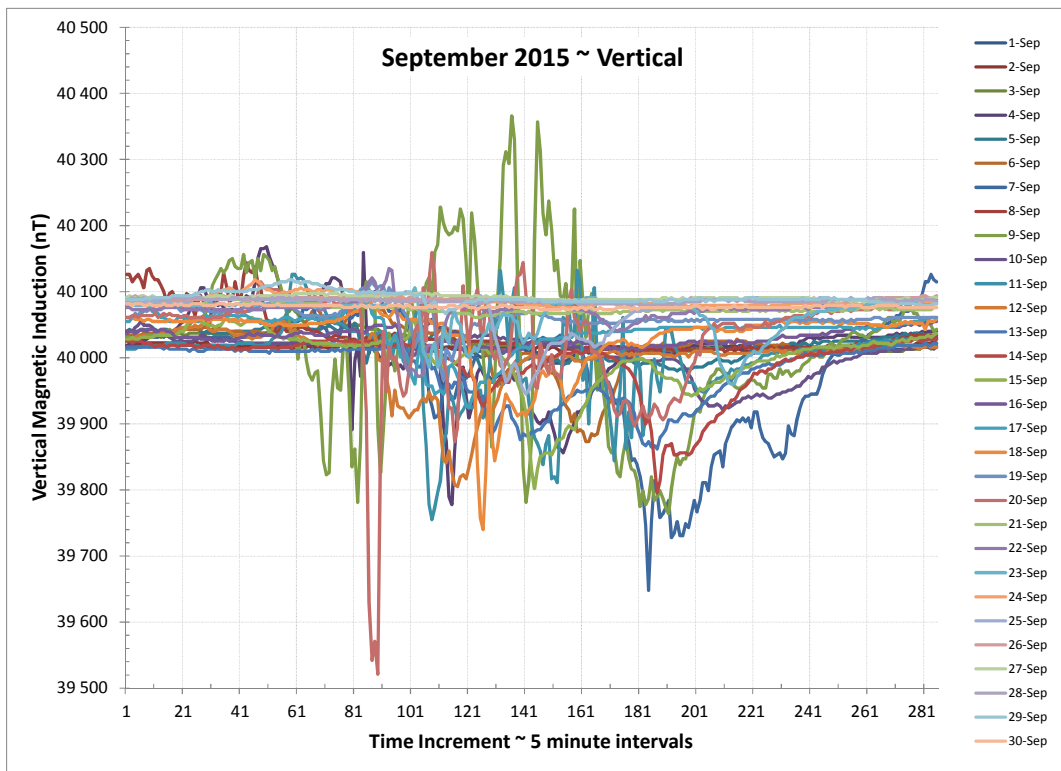
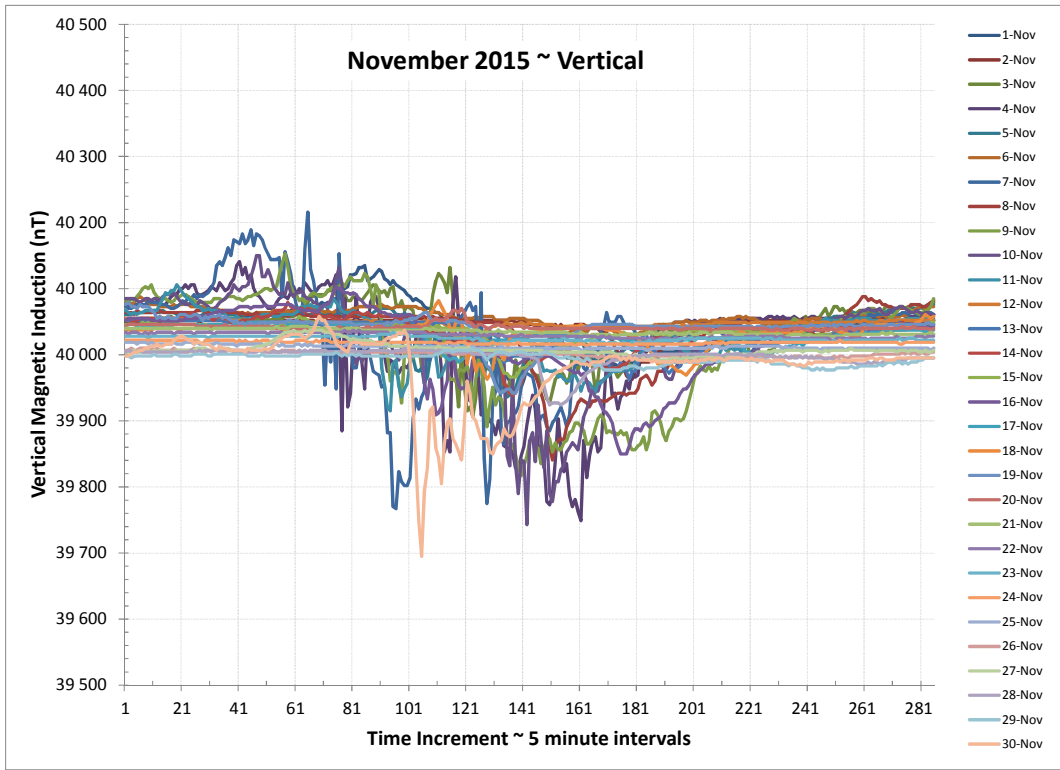


Figure 2.6 ~ Overlays of the daily vertical magnetic flux density plots for each of the three months in the study period. The horizontal time scale on each plot is an index of 5 minute intervals. Major tick marks are at 100 min intervals. The vertical scales are uncalibrated values.



Monthly magnetograms: The daily horizontal magnetic data were concatenated to produce monthly plots (figure 2.7). The monthly plots clearly show the daily variation in the local magnetic field. These daily variations are caused by the strong electric currents circulating in the ionosphere that drift westward as the Sun passes overhead.

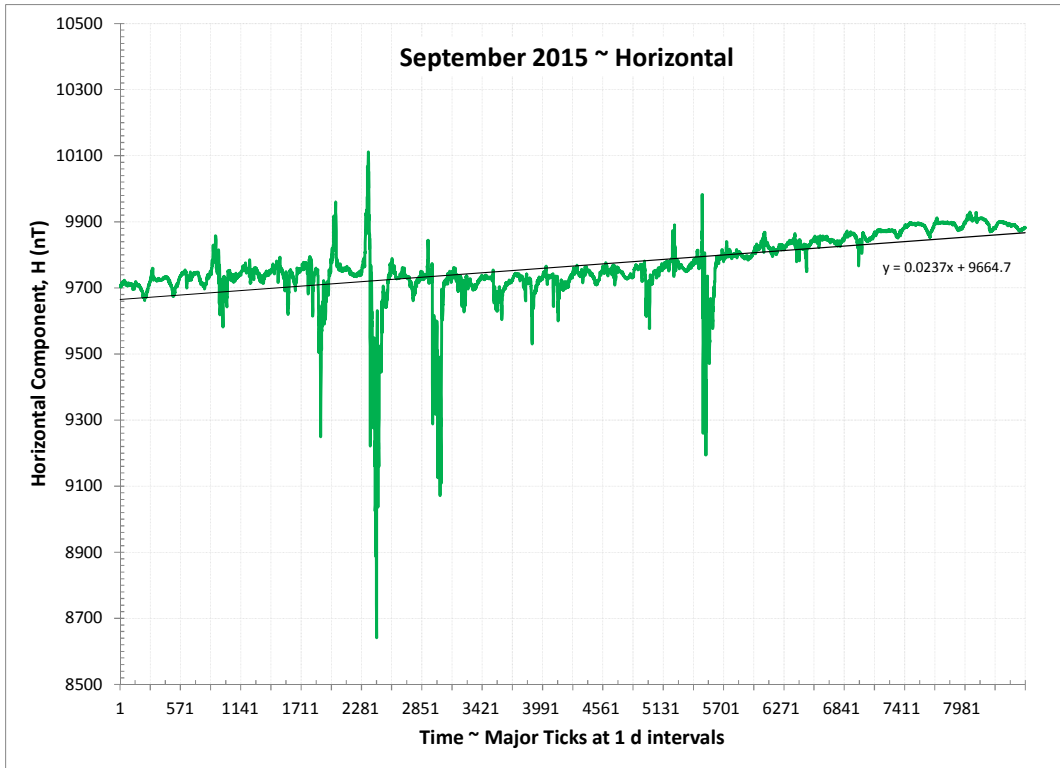
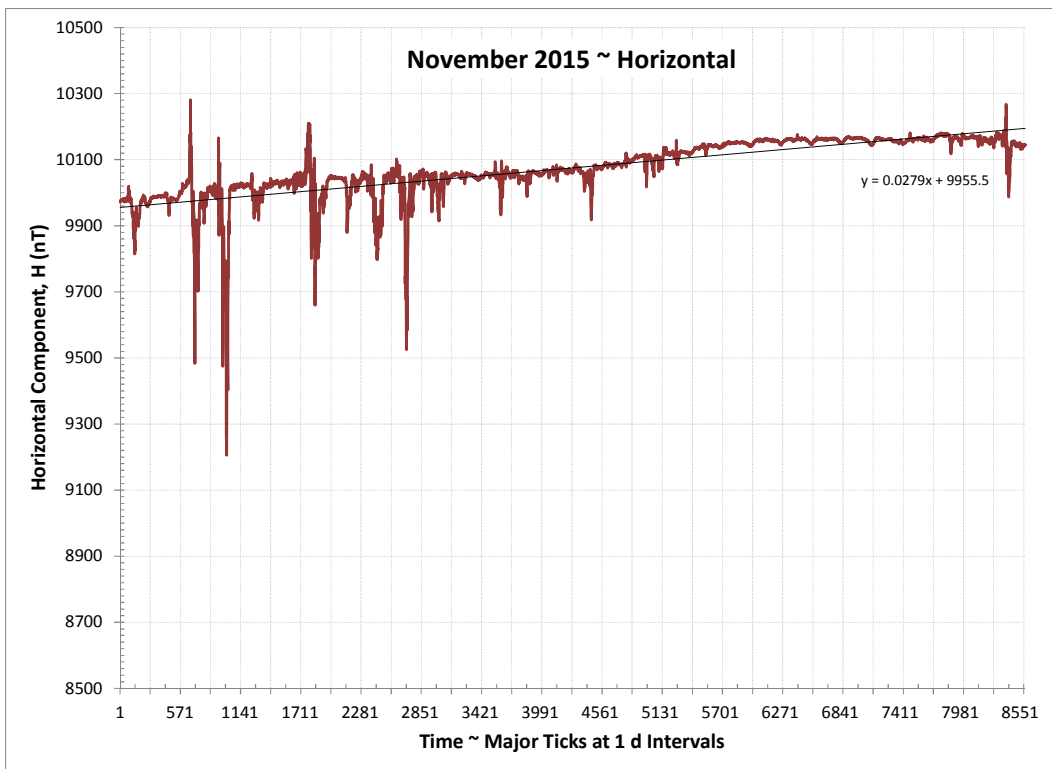
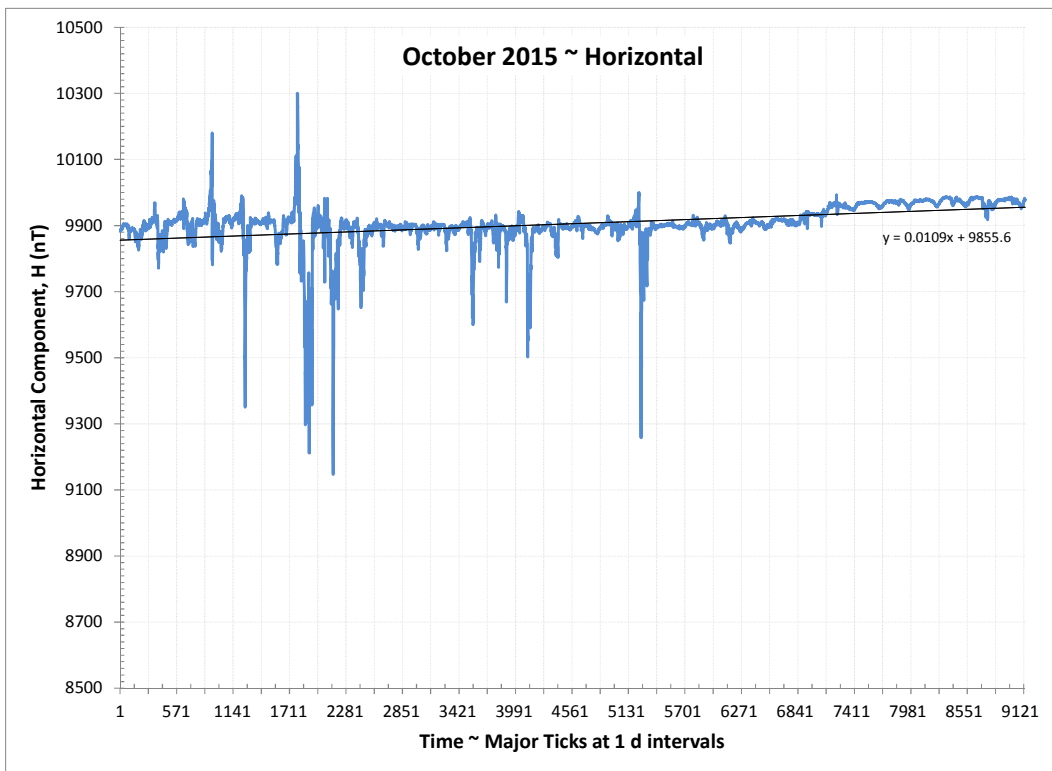


Figure 2.7 ~ Monthly plots of magnetic flux density. The horizontal time scale on each plot is an index of 5 minute intervals with major tick marks set to 1 d interval. The vertical scales are uncalibrated values of the horizontal component (vector sum of B_x and B_y). The slow rise is due to temperature effects.



3-Month Magnetogram showing temperature effects: The magnetic sensors used with the SAM-III are quite sensitive to temperature. The sensors usually are buried in a fixture in soil to eliminate daily temperature variations. Seasonal or long-term temperature variations can be reduced only by burying the fixture at least 3 m (depending on the soil thermal conductivity). The sensors at Anchorage are about 1 m underground. The seasonal temperature changes are manifested as a slow drift upward of the measured magnetic flux density in

the fall and downward in the spring; the former is apparent in the monthly and long term plots (figure 2.8). The long-term plots also clearly show the repetitive nature of disturbances on a 27 d scale, in the case by the space weather from persistent coronal holes that intercept Earth as the Sun rotates.

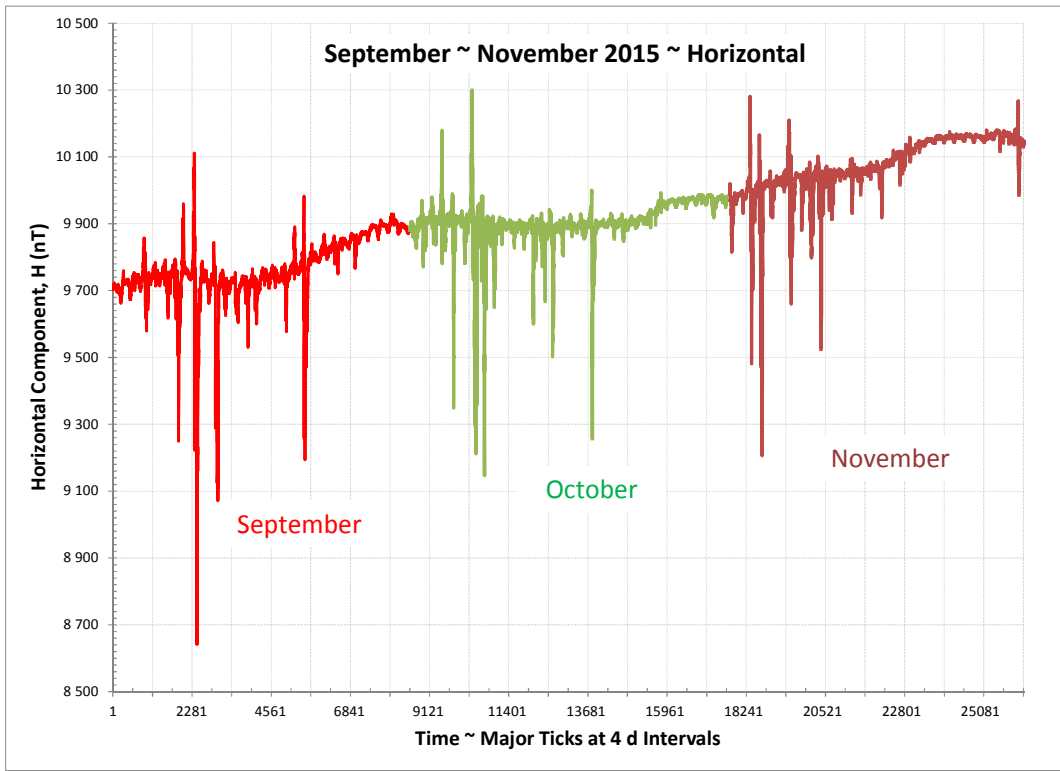


Figure 2.8 ~ The long-term plot is a concatenation of the data for three months. The horizontal time scale on each plot is an index of 5 minute intervals with major tick marks at 1 day intervals. The vertical scales are uncalibrated values of the horizontal component (vector sum of B_x and B_y). Disturbances are seen to repeat with a 27 d period, coinciding with the Sun's rotation.

Cyclic loading and unloading of the magnetotail: As mentioned above, disturbances in the solar wind can transfer energy to Earth magnetic field. This energy moves to the magnetotail where it loads and unloads, sometimes in a cyclic manner. These cyclic disturbances are often observed in daily plots, two of which are shown here (figure 2.9). These cyclic variations may be related to substorms. Substorms are often discussed but poorly defined in geomagnetic literature. They seem to be a phenomenon related to field-aligned currents that enter the polar ionosphere and intensify the auroral electrojet (high latitude ring currents), which causes a perturbation in the magnetosphere.

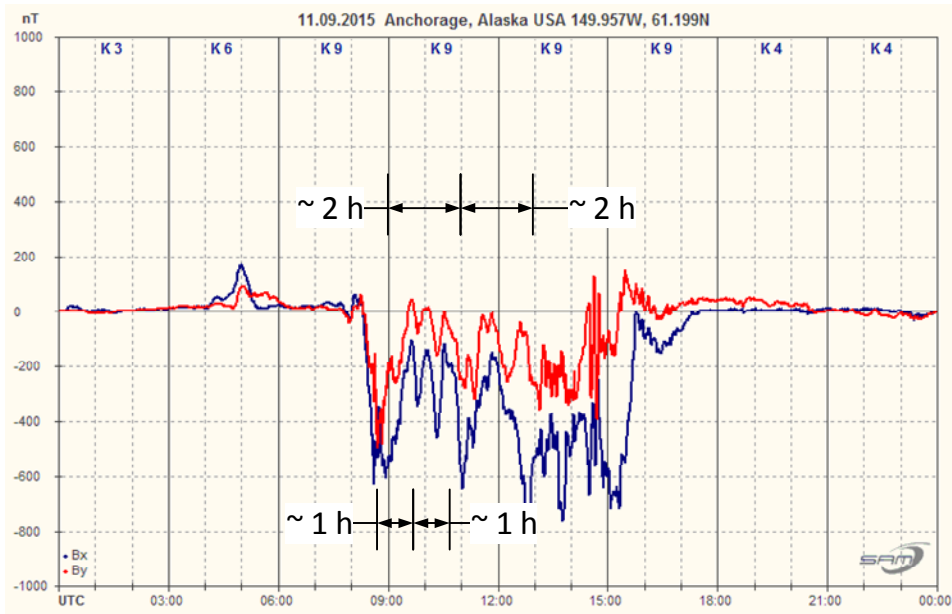
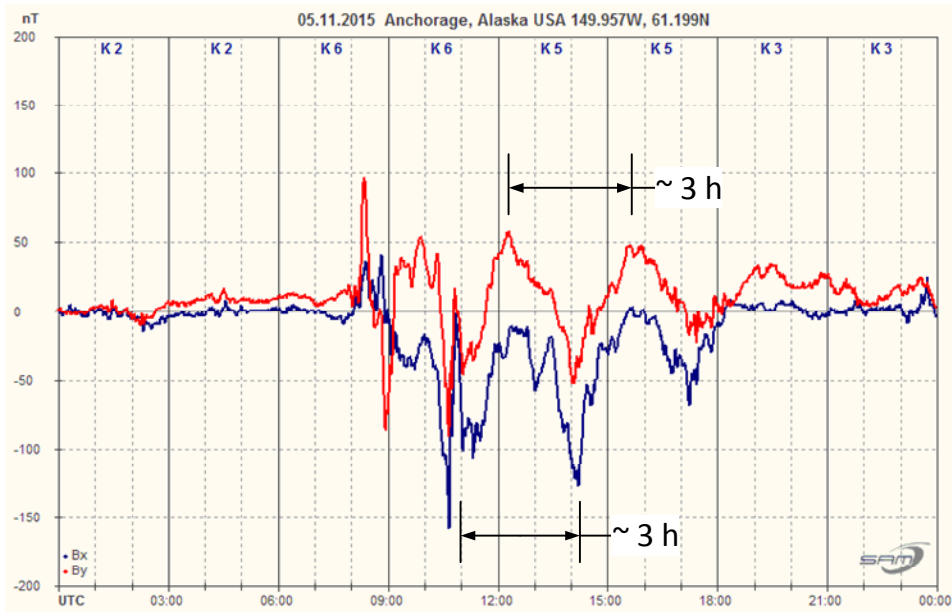


Figure 2.9 ~ Example magnetic flux density plots that show the oscillatory characteristics of Earth's magnetic field at Anchorage, Alaska during or following a disturbance. These oscillations are part of the loading and unloading cycle in Earth's magnetotail during a disturbance. Only B_x and B_y are shown and both usually are affected.



Upper: Oscillations with two different periods can be seen on 11 September, one around 1 h and another around 2 h.

Lower: The oscillations on 5 November have a period of about 3.0 to 3.5 h.

Fourier analysis: Plots of the Fourier coefficients indicate variations corresponding to a period of 24 hours and other times (figure 2.10). As mentioned above, the drifting currents in the sunlit ionosphere affect the magnetic field measured on the surface, so I expected to see periods related to the length of daylight. The average length of daylight for Anchorage, Alaska during the study period was: September ~ 14.25 h; October ~ 11.5 h; November ~ 8.5 h. The Fourier plots show some indications that could be related to the amount of sunlight; however, the daylight hours change rapidly in the fall and the indications simply may be noise resulting from the lack of sophistication in the analysis.

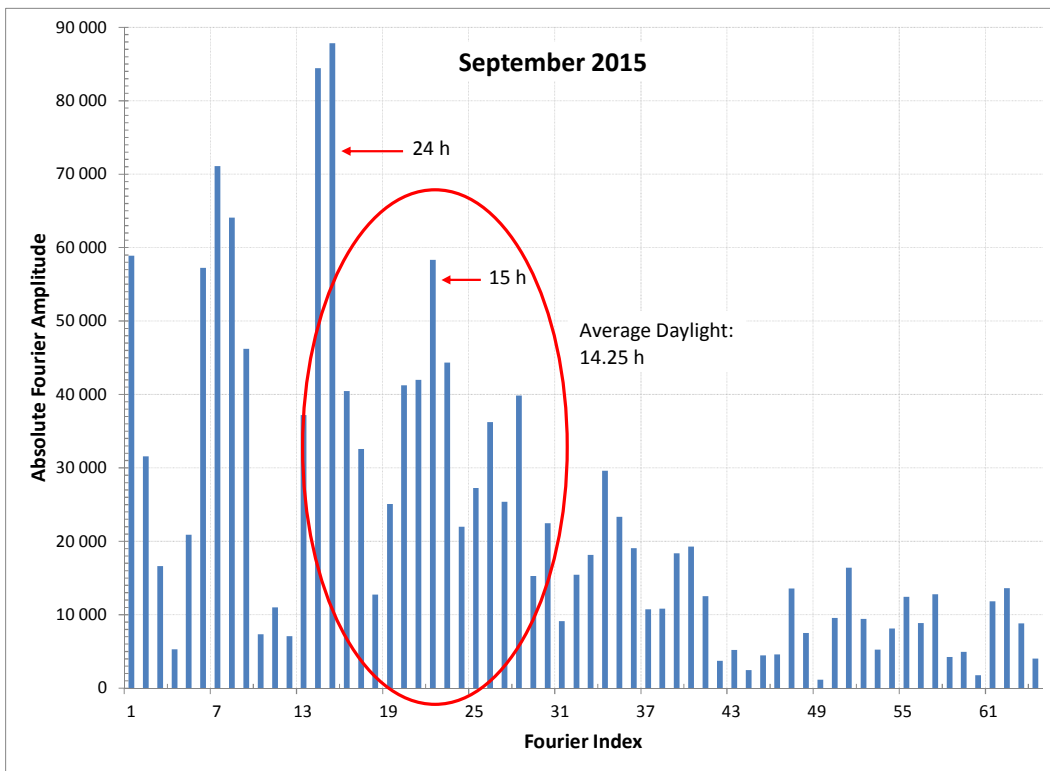
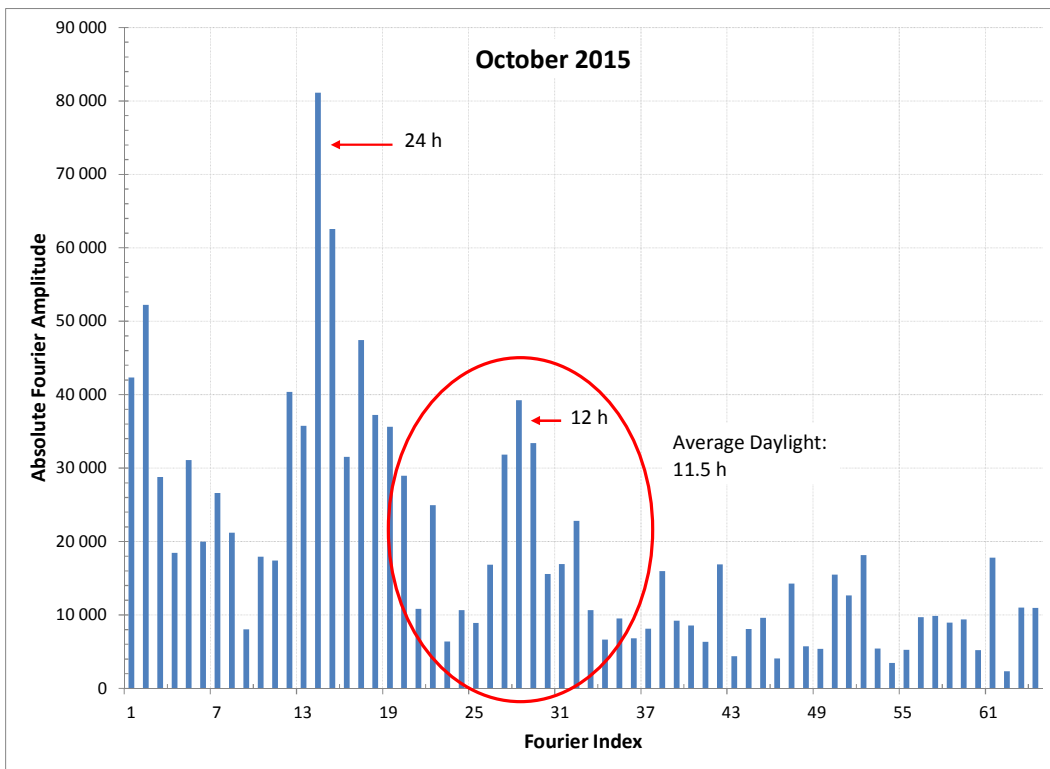


Figure 2.10 ~ Fourier coefficients from the data for each month reveal strong frequencies corresponding to a 24 h period.

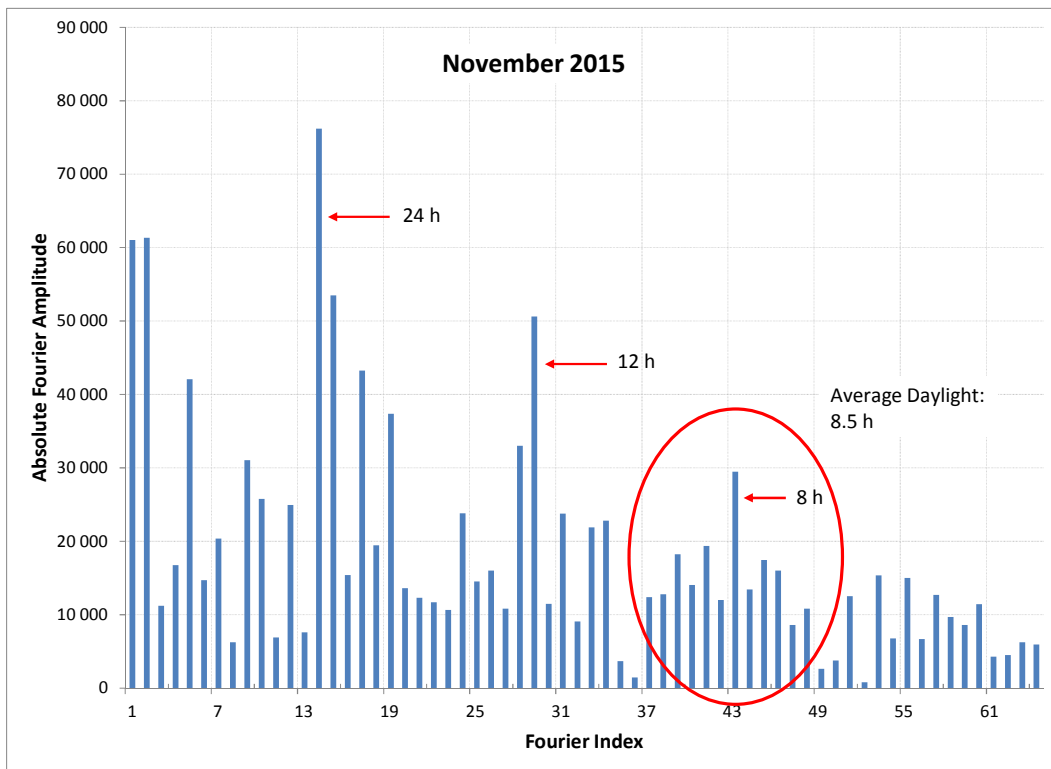
There also may be indications of daylight variations in each of the plots as follows:



15 h for September (14.25 h actual average)

12 h for October (11.5 h actual average)

8 h for November (8.5 h actual average).



2.4 Selected Events

Almost all geomagnetic disturbances during the 3-month study period were caused by a corotating interaction region accompanied by a coronal hole high-speed stream but there were several solar sector boundary crossings and CME events as well. The following descriptions cover a few selected events during the study period and include the Anchorage magnetogram and corresponding WSA-Enlil model image for comparison (only the first model image is annotated). Information from Space Weather Prediction Center weekly report and summary *also* are included for most of these events.

4 October 2015: A geomagnetic disturbance occurred on 4 October when the magnetic flux density at Anchorage began to rise at about 0300 (figure 2.11) from a corotating interaction region. The disturbance began about 0300 when the flux density started to rise rapidly. A major storm was then indicated about 0600 and lasted until about 1800. The WSA-Enlil model indicated a peak in plasma density from the CIR at 1200 while the radial velocity due to a coronal hole rose to peak levels over the next 12 hours. Adding to the disturbances was a glancing blow from a CME. SWPC reported periods of southward B_z at the ACE spacecraft and localized substorms.

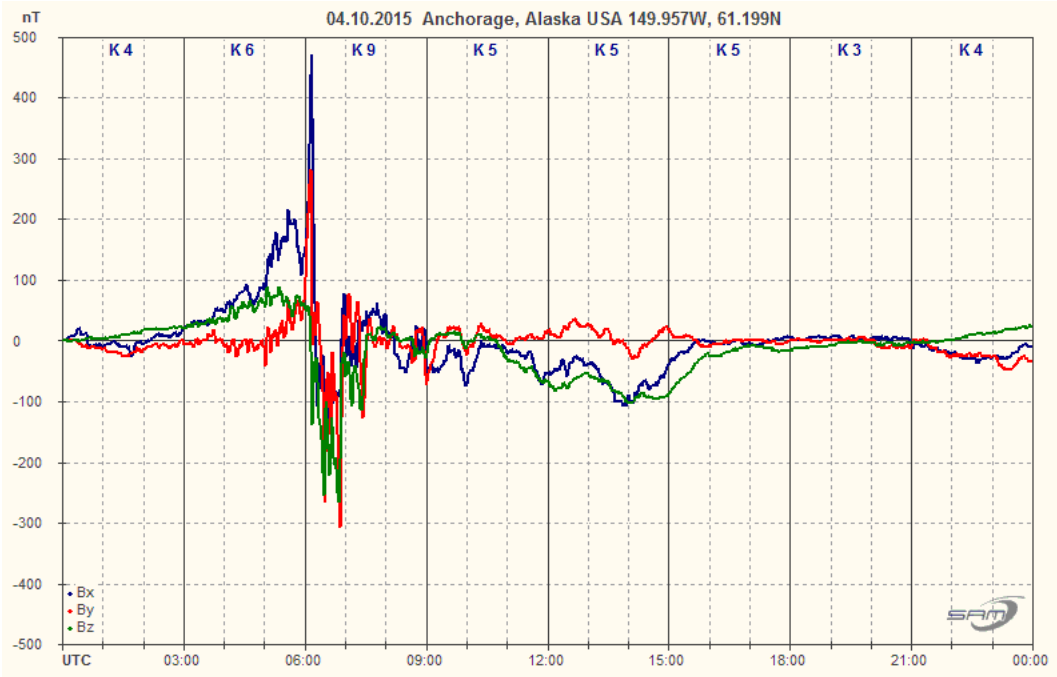
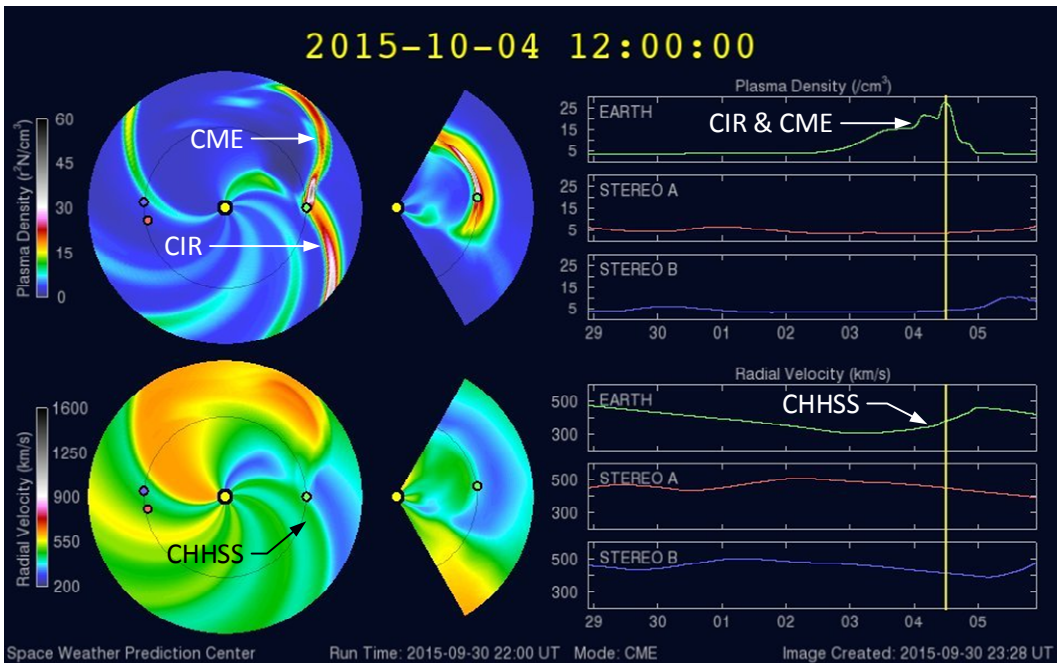


Figure 2.11 ~ Combination event caused by a CIR, CHSS and CME.

Upper: Magnetic flux density over the 24 h period of 4 October, reflecting the effects of a corotating interaction region followed by a coronal hole high-speed stream mixed with a coronal mass ejection.



Lower: The WSA-Enlil model for 4 October indicates the effects of the CIR (plasma density), CHSS (radial velocity) and CME (both).

18 October 2015: Solar sector boundary crossing combined with an equatorial positive polarity coronal hole high-speed stream followed by prolonged southward B_z (figure 2.12). SWPC reported solar wind speed peaked at the ACE spacecraft at 480 km/s about 1800 and total field peaked at 12 nT. The B_z component reached -8 nT (southward) about 0800.

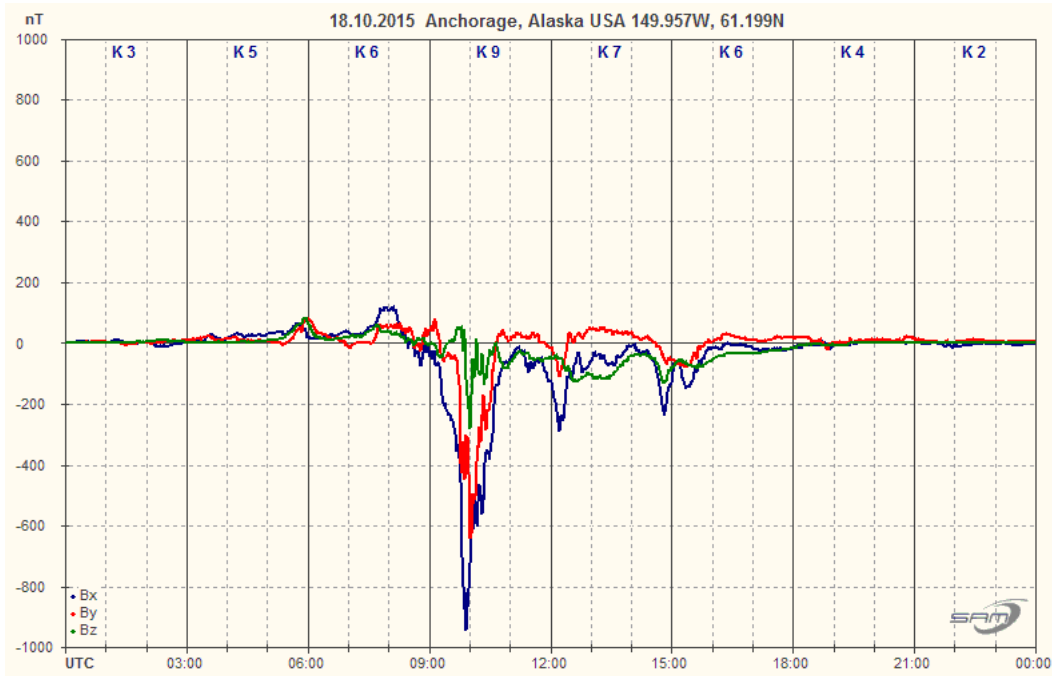
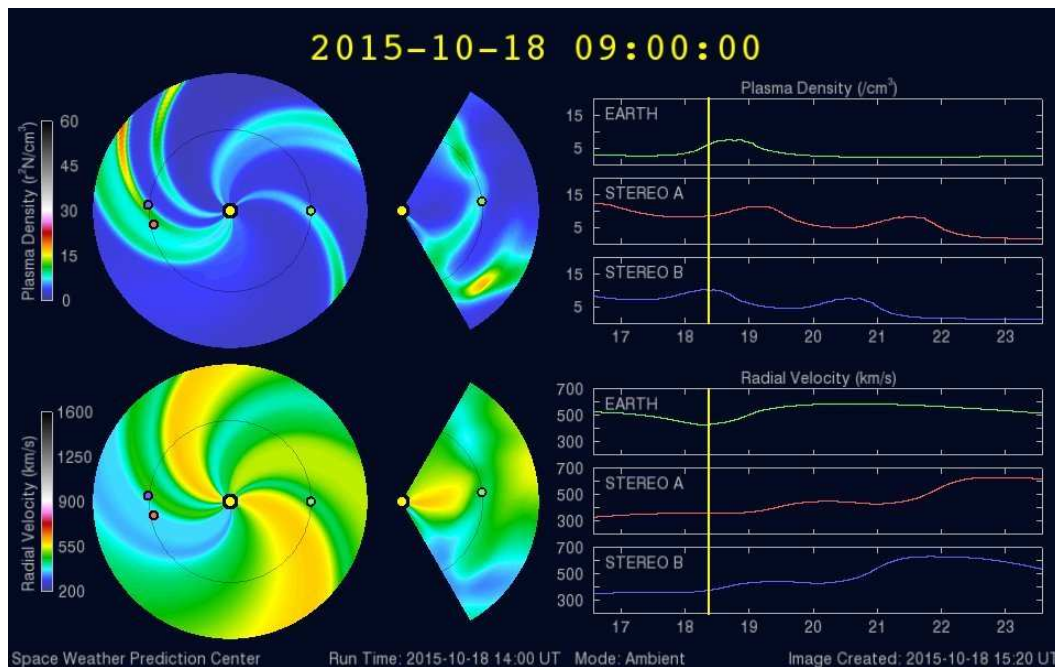


Figure 2.12 ~ SWPC (edited): Solar wind parameters reflected a nominal solar wind regime early in the period but became enhanced after 0000 UTC. Solar wind speeds slowly increased from initial values near 350 km/s to end-of-period values near 430 km/s. IMF total field values reached a peak of 12 nT and B_z reached a maximum southward deflection of -11 late in the period. The ϕ angle was variable throughout the period. The geomagnetic field was at quiet to active levels until 0900-1200 UTC when planetary G1 (Minor) geomagnetic storms were observed.



24 October 2015: Normal solar wind parameters prior to arrival of a CME (figure 2.13). SWPC reported the CME that occurred from NOAA AR 2434 on 22 October arrived at ACE spacecraft on 24 October at 1828 followed by enhanced solar wind speed but otherwise had only minor effects on the geomagnetic field.

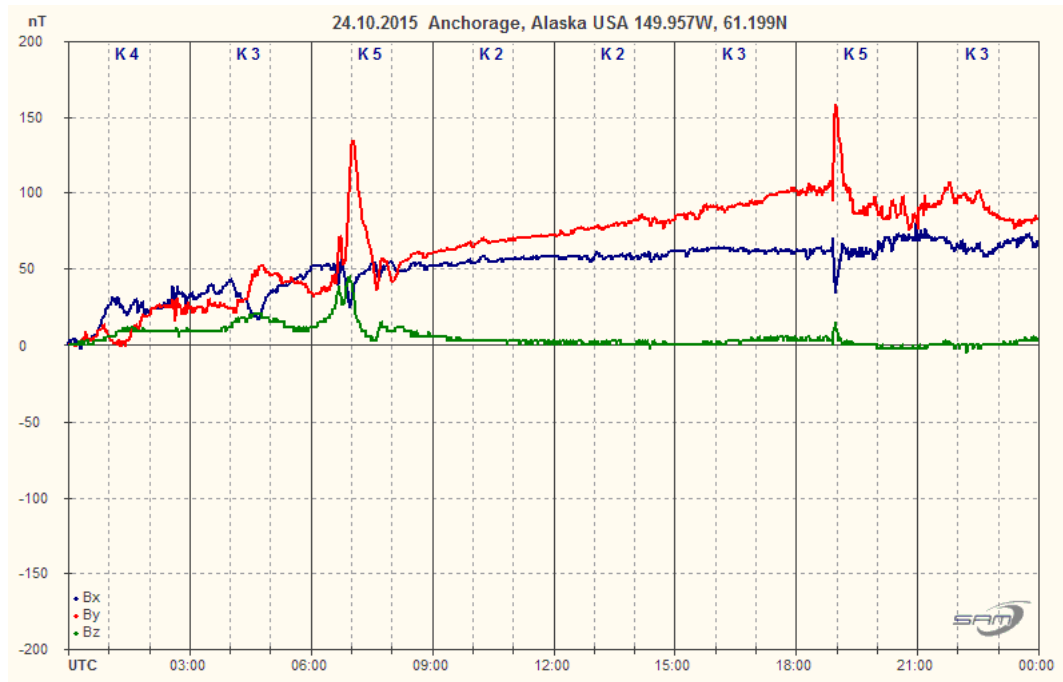
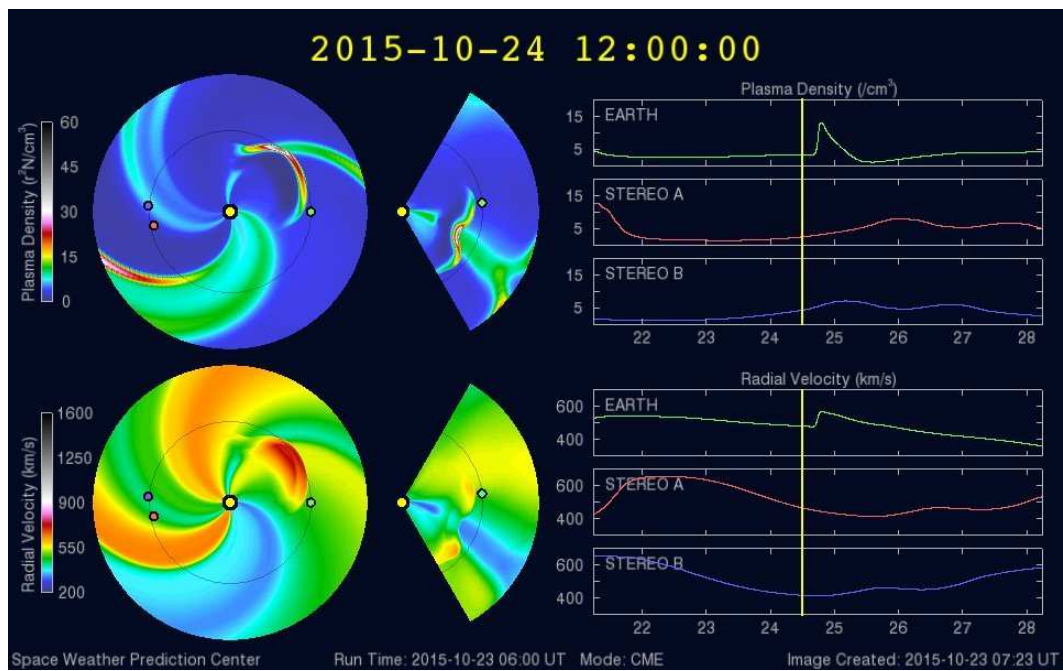


Figure 2.13 ~ SWPC (edited): Solar wind parameters were at background levels throughout the period. Solar wind speeds were steady between 420-480 km/s and B_z was predominately northward with only brief excursions southward. The phi angle transitioned from a negative (toward) solar sector to a positive (away) sector orientation after 0800 UTC.



3 November 2015: Equatorial positive polarity coronal hole high-speed stream preceded by a corotating interaction region (figure 2.13). SWPC reported the solar wind speed measured at the ACE spacecraft increased and the total field B_T increased to a peak of 34 nT at 0700 while the B_z component reached a maximum southward value of -24 nT at 0620.

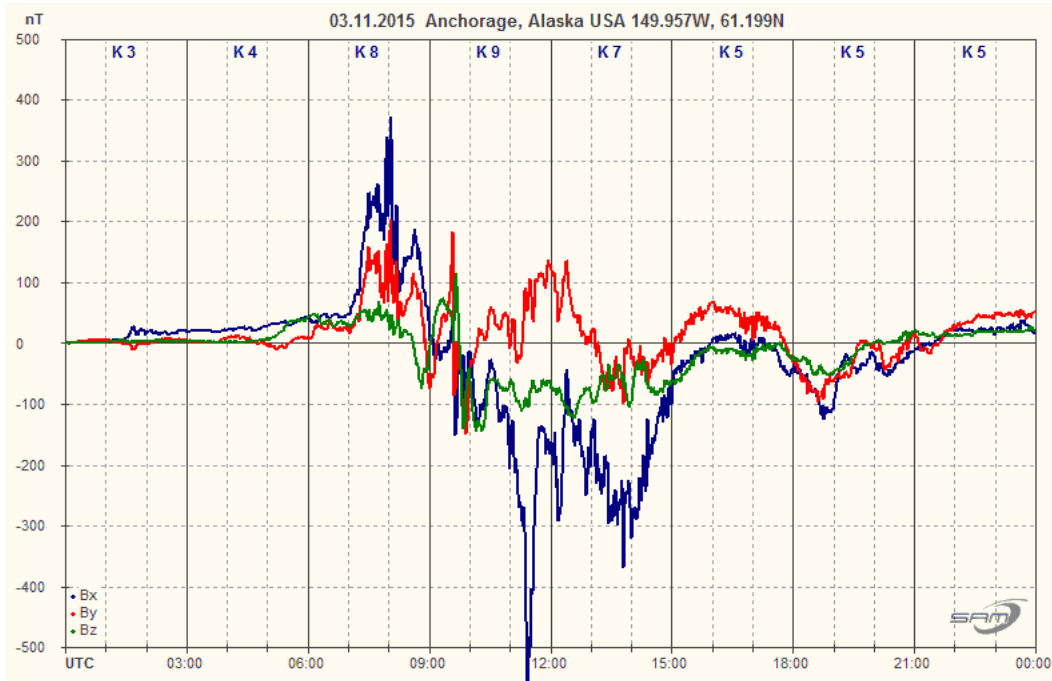
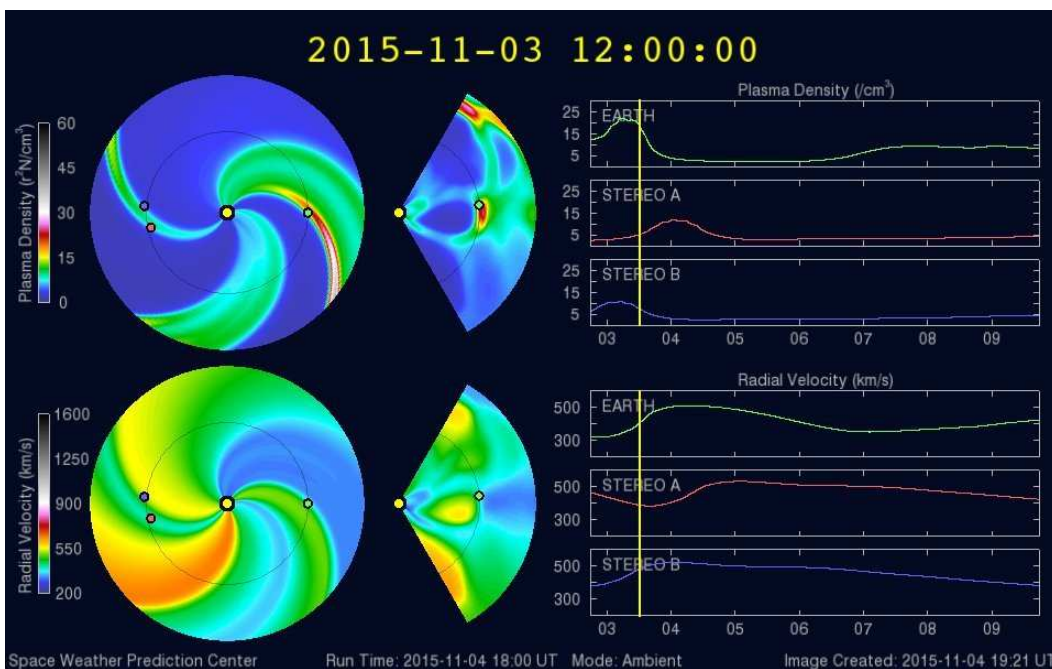


Figure 2.14 ~ SWPC (edited): Solar wind parameters, as measured by the ACE spacecraft, remained at nominal levels for the first half of the period. At about 2214 UTC, B_T reflected a pronounced jump from around 3 nT to 10 nT. This was followed by an increase in solar wind speed from ~ 320 km/s to ~ 410 km/s and an increase in density. Conditions remained slightly enhanced until approximately 0530 when B_T jumped from 4 nT to 22 nT, B_z dropped from -5 nT to -24 nT, and wind speeds began to increase. B_T reached a peak of 37 nT while B_z saw a maximum southward deflection to -24 nT. Wind speed saw a brief increase to near 700 km/s and remained steady near 665 km/s. The geomagnetic field increased from quiet to minor (G1-Minor) storm levels early in the period as the anticipated CIR began to influence Earth's magnetosphere.



14 November 2015: Corotating interaction region followed by positive polarity coronal hole high-speed stream (figure 2.15). SWPC reported solar wind speeds at the ACE spacecraft in the upper 400 km/s range and that total field ranged from 5 to 9 nT.

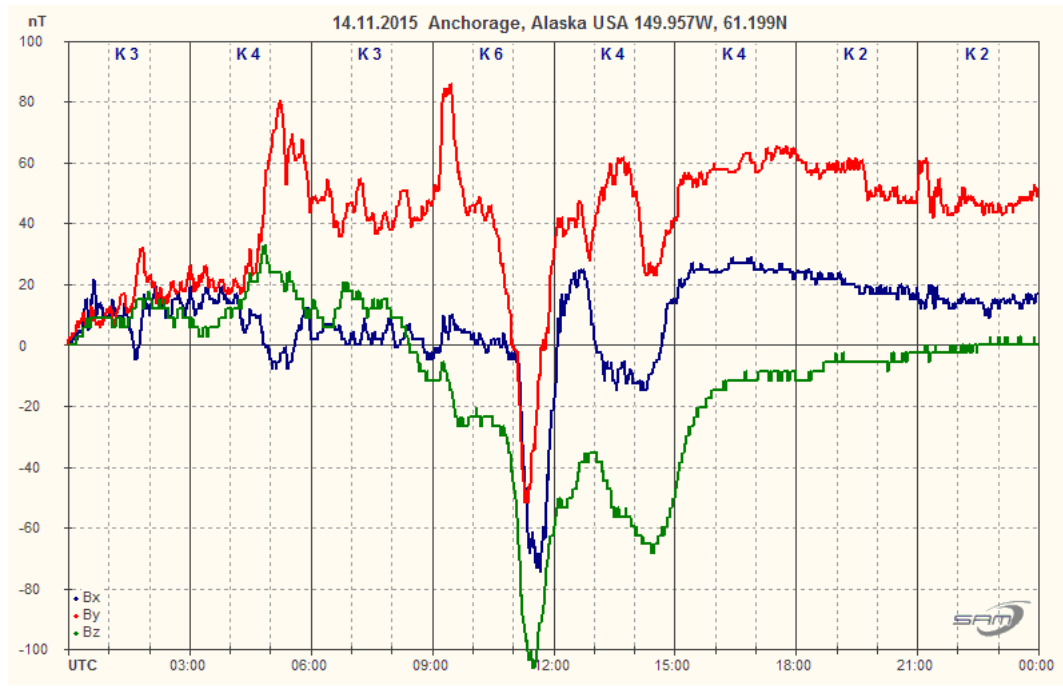
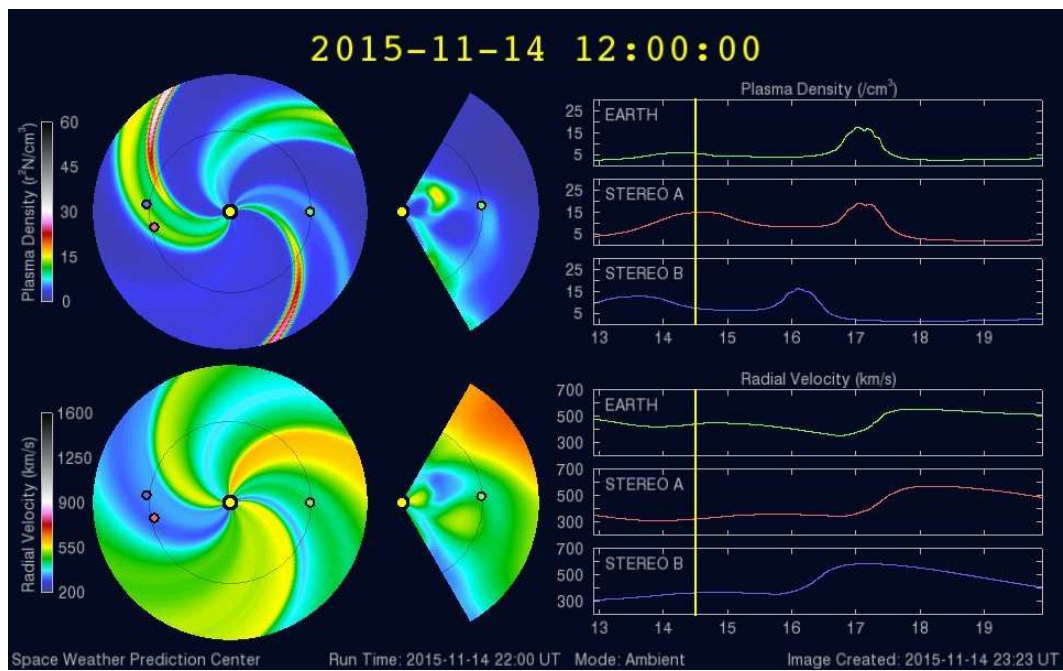


Figure 2.15 ~ SWPC (edited): Solar wind parameters indicated the likely onset of a CIR followed by the influence of a positive polarity CHSS. Solar wind speeds slowly increased from 405 km/s to ~480 km/s through about 1800. Winds speeds of 460 km/s to 480 km/s persisted through the end-of-the-period. IMF B_T reached 11 nT by about 1430 UTC before tailing off to 3 nT by periods end. The B_z component reached a maximum southward deflection of -8 nT between 1300-1500 UTC, but finished the period variable between ± 2 nT. The ϕ angle was generally positive (away from the Sun). The geomagnetic field was at quiet to active levels under the influence of the positive polarity CHSS.



30 November 2015: Corotating interaction region followed by positive polarity coronal hole high-speed stream (figure 2.16). SWPC reported normal conditions at the ACE spacecraft for 30 November.

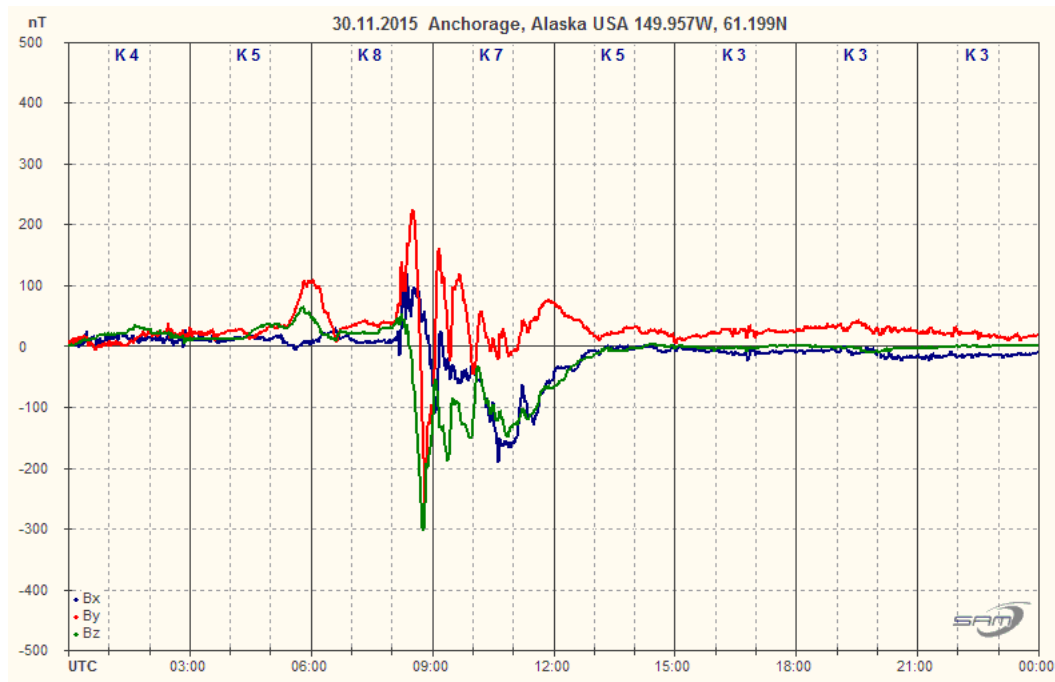
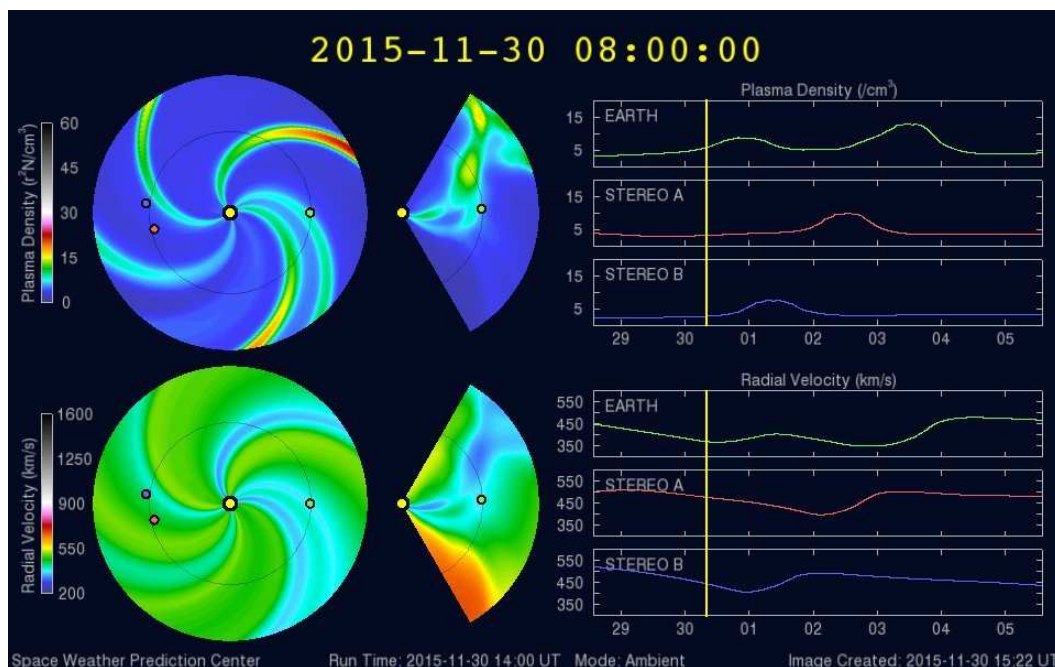


Figure 2.16 ~ SWPC (edited): Solar wind parameters indicated arrival of a CIR followed by a CHSS. For the majority of the period B_T was between 1 nT and 11 nT with the B_z component mostly negative near -5 nT after 1749. By 0612, total field began to increase to a maximum of 15 nT with a maximum southward B_z around -13 nT. By end of the period, B_T decreased to around 8 nT. Near 0810 solar wind speeds increased to ~520 km/s. Phi angle was variable throughout the period until 0630 when it settled into mostly positive (away) sector. The geomagnetic field was at quiet to G1 (Minor) storm levels over the period due to the onset of a CIR and subsequent CH HSS activity. An isolated G1 (minor) storm period was observed during the 30/0600-0900 UTC period as the CIR began influencing the geomagnetic field.



2.4. Conclusions

The geomagnetic activity observed at Anchorage, Alaska during the autumn of 2015 varied from very quiet to severe storm levels as Earth's magnetosphere was affected by space weather including coronal hole high-speed streams, coronal mass ejections, corotating interaction regions and solar sector boundary crossings. Of the 728 3-hour synoptic periods during that time about 29% experienced storm levels defined for purposes here as a K-index of K5 or greater. There were no known deleterious terrestrial effects of these storms.

2.5. References and Further Reading for Part II

- [ReeveSI] Reeve, W., Geomagnetic Sudden Impulses, 2013, available here:
http://www.reeve.com/Documents/Articles%20Papers/Observatoins/Reeve_GeomagSuddenImpulses.pdf
- {GeoMag} Reeve, W., Geomagnetism Tutorial, 2011, available here:
<http://www.reeve.com/Documents/SAM/GeomagnetismTutorial.pdf>
- Knipp, D., Understanding Space Weather and the Physics Behind It, Space Technology Series, Learning Solutions, McGraw-Hill Book Co., 2011
- Moldwin, M. An Introduction to Space Weather, Cambridge University Press, 2008

Document information

Author: Whitham D. Reeve

Copyright: © 2016 W. Reeve

Revision: 0.0 (Original draft started, 14 Sep 2015)
0.1 (Added CIR, SSBC and latitude variations, 21 Sep 2015)
0.2 (Edited ACE, 03 Oct 2015)
0.3 (Minor edits, 14 Oct 2015)
0.4 (Added IMF section, 4 Nov 2015)
0.5 (Added LASCO images and revised images, 5 Nov 2015)
0.6 (Added magnetograms and text in Part II, 22 Dec 2015)
0.7 (Added observation images and cleaned up text, 24 Dec 2015)
0.8 (Worked on completion of 1st draft, 25 Dec 2015)
0.9 (Final work on 1st draft, 27 Dec 2015)
1.0 (2nd draft, added z-component plots, 10 Jan 2016)
1.1 (Cleanup Part I, 12 Jan 2016)
1.2 (Final cleanup, 16 Feb 2016)
2.0 (Distribution, 17 Feb 2016)
2.1 (Added reconnection details, 05 Apr 2016)

Word count: 7299

File size: 18748416